Remote Sensing of Environment 204 (2018) 162–180

Contents lists available at ScienceDirect

Remote Sensing of Environment

journal homepage: www.elsevier.com/locate/rse

X-, C-, and L-band SAR signatures of newly formed sea ice in Arctic leads during winter and spring

A. Malin Johansson[a,*], Camilla Brekke[a], Gunnar Spreen[b,c], Jennifer A. King[c]

[a] Department of Physics and Technology, UiT The Arctic University of Norway, Tromsø, Norway
[b] University of Bremen, Institute of Environmental Physics, Bremen, Germany
[c] Norwegian Polar Institute, Tromsø, Norway

ARTICLE INFO

Keywords:
Sea ice
SAR
Polarimetry
Multi-frequency

ABSTRACT

We examine an extensive synthetic aperture radar (SAR) data set from the Arctic Ocean spanning a time period from January to June 2015, with the aim of identifying multi-polarization parameters that can be used to accurately separate newly formed sea ice from the surroundings. Newly formed sea ice areas both provide favourable routing for ship traffic, and are key to Arctic climate science because they enable heat exchange between the ocean and the atmosphere. Our data set encompasses three different frequencies, X-, C- and L-band, at a range of incidence angles, and were acquired under different environmental conditions. Our results suggest that by combining the scattering entropy and the co-polarization ratio we can successfully separate the newly formed sea ice from open water and thicker sea ice within all three frequencies throughout the winter and spring season. We observe a high correlation between scattering entropy values calculated using quad-polarization C- and L-band data and scattering entropy values calculated using the same scenes reduced to the co-polarization channels (HH and VV). We therefore conclude that dual-polarization (HH and VV) X-band scenes can be directly used to complement quad-polarimetric C- and L-band scenes for studies of newly formed sea ice. To confine the quad-polarimetric data sets to their co-polarization channels one can ensure a higher signal-to-noise ratio. Incidence angles below 35° are needed to keep the signal-to-noise ratios sufficiently high for the scattering entropy and co-polarization ratio. Due to its lack of incidence angle dependency, the polarization difference can provide additional support in newly formed sea ice studies. The regular coverage of the Arctic Ocean with C-band SAR means that such scenes should to be included in any automatic monitoring, however, X- and L-band SAR can, based on their difference in penetration depth, provide additional information about newly formed sea ice types and surface structure.

1. Introduction

Maritime activities in the Arctic region mean routing and operations within ice infested areas. Areas with newly formed sea ice or open water, such as leads, are important for a more cost-effective passage through the ice. They are also important for energy exchange between the ocean and the atmosphere and can permit transmission of enough light into the ocean to initiate and sustain algae blooms in regions where otherwise the consolidated ice cover wouldn't allow (Assmy et al., 2017). Synthetic aperture radar (SAR) satellite scenes offer spatial resolutions down to the meter scale and are independent of light and clouds. Due to this all-season capability SAR is widely used for sea ice monitoring and C-band SAR has traditionally been used to monitor sea ice extent, concentration, drift speed and ice type, e.g., Maillard et al. (2005), Thomas et al. (2011), and Walker et al. (2006). Work by, e.g., Casey et al. (2016), Dierking and Busche (2006), Eriksson et al. (2010), and Lehtiranta et al. (2015) has identified that other SAR frequencies can contribute useful information for sea ice classification where Casey et al. (2016) investigated how L-band SAR can contribute to sea ice type products during the melt season. Using X-, C- and L-band SAR satellite data in combination allows us to utilise the multiple missions currently available (Johansson et al., 2017).

In addition to SAR sensors, passive microwave sensors have been used to estimate newly formed sea ice thickness as well as to study the sea ice freeze-up. Notably work by, e.g., Kaleschke et al. (2012) focused on the initial growth in the freeze-up period, Markus et al. (2009) used a time series to assess changes in the freeze-up, and work by Martin et al. (2004) focused in thin ice thickness estimates.

With respect to SAR studies, e.g., Zakhvatkina et al. (2017), have shown that dual or quad polarimetric SAR is needed to accurately

* Corresponding author.
E-mail address: malin.johansson@uit.no (A.M. Johansson).

http://dx.doi.org/10.1016/j.rse.2017.10.032
Received 15 April 2017; Received in revised form 2 October 2017; Accepted 18 October 2017
Available online 02 November 2017

identify and separate the newly formed sea ice from the surrounding thicker sea ice. Here we define *newly formed sea ice* as the thinnest ice categories including new ice (frazil, grease and slush), nilas (0.05–0.10 m thick), and young ice (0.10–0.30 m thick) (WMO, 1970). Identifying a set of SAR parameters that can be used for identification of newly formed sea ice and separating it from other ice types under varying temperature and incidence angle conditions is the scope of this work. The availability of a temporally extensive multi-frequency SAR data set with acquisitions in X-, C- and L-band, respectively, allows a comprehensive study comparing the frequency dependent radar response to sea ice under varying temperature and incidence angle conditions. The parameters and their variability with temperature and incidence angle can then be used as additional information for manual sea ice chart products as produced by ice services around the world, and as input into automatic sea ice type analysis.

Fully polarimetric satellite scenes typically have a small areal coverage, though enables high resolution parameter retrieval. To enable both high spatial coverage and increased amount of polarimetric information, the compact polarimetry (CP) SAR mode was introduced (Raney, 2007). Works by, e.g., Dabboor and Geldsetzer (2014) and Geldsetzer et al. (2015), have demonstrated its usability for polarimetric sea ice observations where the latter study also focused on newer sea ice types. Some of the compact polarimetry parameters investigated in those studies have corresponding fully polarimetric parameters used in this study, e.g., the Stokes vector second component (from CP) is similar to the polarization difference and the right co-polarized ratio (from CP) is similar to the co-polarization ratio assuming reflection symmetry and reciprocity. The right co-polarized ratio is defined as the ration between right circular on transmit, horizontal on receive and right circular on transmit, vertical on receive, RH/RV. Moreover, the degree of polarization (from CP) is similar to the scattering entropy (Cloude et al., 2012). In Geldsetzer et al. (2015), separation between newly formed sea ice and multi-year ice was possibly using, e.g., the degree of polarization. Results by Espeseth et al. (2017) comparing RISAT-1 compact polarimetry data and Radarsat-2 full polarimetry data measurements have shown that the compact polarimetry and full polarimetry can be comparable. Recent and upcoming compact polarimetry SAR missions includes C-band missions, such as RISAT-1 (ended) and RADARSAT Constellationmission (upcoming), and L-band missions, such as ALOS-2 (ongoing) and ALOS-4 (upcoming). These missions will enable multi-frequency sea ice studies using compact polarimetry. This study, however, is confined to conventional coherent linear on transmit and linear on receive SAR systems.

The manuscript is organised as follows. Section 2 gives a review of previous related studies. Section 3 describes the experimental setup and the data collection. Satellite data processing and extracted polarimetric information is introduced in Section 4. A multi-sensor analysis is presented in Section 5 and in Section 6 implications for operational monitoring of sea ice is discussed, followed by conclusions in Section 7.

2. Background and previous studies

Dual-polarization SAR data has, when available, been preferred to single polarization data due to easier separation between different sea ice types (Dierking, 2010; Sandven et al., 2008). Furthermore, dual-polarization data can be used to differentiate between open water and sea ice, e.g., Scheuchl et al. (2004), Arkett et al. (2006), and Geldsetzer and Yackel (2009), and are used by operational services around the world for this purpose. Dual-polarization has primarily consisted of the following combination; HH and HV. The first letter refers to the transmitted polarization and the second the received polarization. The cross-polarization channels (HV and VH) have been identified as an important asset for improved sea ice classification (Dierking, 2010). One reason for this is the reduced incidence angle dependence on the backscatter for these two channels compared to the co-polarization channels (HH and VV). The HV and VH channels have lower backscatter values and are closer to the noise floor than the HH and VV channels. Using spacebourne SAR data, Partington et al. (2010) concluded that for newly formed sea ice studies the HV-channel was only useful for incidence angles below 30° due to the signal's proximity the noise floor. Using airborne L-band SAR, Wakabayashi et al. (2004) concluded that incidence angles < 45° were needed to differentiate between different sea ice types due to the low signal-to-noise ratio (SNR) of the HV-channel.

Dual-polarization SAR satellite products with a combination of the two co-polarization channels HH and VV, have been found particularly useful for newly formed sea ice separation from surrounding ice (see Ressel and Singha, 2016 and references therein). The TerraSAR-X satellite has experimental quad-polarization capabilities (Ressel and Singha, 2016; Johansson et al., 2017) but also offers the HH/VV combination as an option for the standard dual-polarization acquisitions. From this follows that the backscatter values from the respective co-polarization channels can be used for identification of different sea ice classes, and such identification can then be complemented and improved by also calculating parameters such as the co-polarization ratio and the polarimetric difference. Making use of quad-polarimetric SAR, Dierking and Wesche (2014), Gill et al. (2013), Wakabayashi et al. (2004), Wakabayashi and Sakai (2010), and Wakabayashi et al. (2013), investigated the value of retrieving information about scattering mechanisms for sea ice classification. Combining the polarimetric information related to the scattering mechanisms and the variation in the radiometry of the backscatter signal of the sea ice enables us to further exploit the possibilities that quad-polarimetric SAR offers for sea ice identification and classification. Substantial work investigating polarimetric responses from SAR sensors mainly operating at C-band has been done by, e.g., Drinkwater et al. (1991), Geldsetzer and Yackel (2009), and Gill et al. (2013), though these studies have mainly focused their efforts towards first-year and multi-year sea ice.

Geophysical parameters such as the dielectric constant and the surface roughness affect the SAR signal over sea ice. In addition, is the backscatter signal affected by the imaging configuration, i.e., the incidence angle (see, e.g., Gill and Yackel, 2012; Lundhaug, 2002; Shokr, 2009; Zakhvatkina et al., 2013), the SAR frequency, the resolution, and the polarization.

2.1. Polarimetric effects on sea ice thickness and type

During initial sea ice growth the backscatter HH and VV intensity values (σ^0_{HH} and σ^0_{VV}) increase with thickness (Nghiem et al., 1997). For C- and L-band, the backscatter values increase by 6–10 dB when the thickness increases 0.03 m (Nghiem et al., 1997). These backscatter changes are also reflected in the co-polarization ratio ($\sigma^0_{VV}/\sigma^0_{HH}$), where an increased thin ice thickness was correlated with a decrease in co-polarization ratio, e.g. Brath et al. (2013), Dierking (2010), Drinkwater et al. (1991), Geldsetzer and Yackel (2009), Kern et al. (2006), Nakamura et al. (2005), Nghiem and Bertoia (2001), Onstott (1992), Wakabayashi et al. (2004), Winebrenner and Farmer (1995), and Zhang et al. (2016). Kern et al. (2006) found that for a sea ice thickness above 0.6 m the co-polarization ratio approaches 0 dB in C-band SAR. L-band SAR studies by Wakabayashi and Sakai (2010) and Wakabayashi et al. (2013) linked changes in scattering entropy to sea ice thickness when the sea ice was less than 0.6 m thick. Dierking and Wesche (2014) observed that young ice and rafted thin ice areas also have lower scattering entropy values compared to the surrounding thicker sea ice.

The change in the backscatter values in response to an increase in thickness also relates to the incidence angle used during the study. Onstott (1992) and Wakabayashi et al. (2004), among others, found that for incidence angles above 40° the decline in co-polarization ratio with increased sea ice thickness were more pronounced than for incidence angles below 40°. A higher incidence angle may therefore be beneficial for separation of newly formed sea ice from the surroundings. However, a study by Partington et al. (2010) found that newly formed

sea ice separation from the open water areas benefited from a lower incidence angle. When assessing the impact on the incidence angle it is also important to keep in mind that different types of newly formed sea ice have different backscatter signature. Beaven et al. (1993) observed a difference of 4 dB in the VV-channel between dark and light nilas and Alexandrov et al. (2004) found that pancake ice had higher backscatter values than nilas. This is in line with a study by Geldsetzer and Yackel (2009) where they found that thin ice showed more variation in the co-polarization ratio than first year ice and multi-year ice.

In this paper, we study the relationship between the polarimetric response from newly formed sea ice with respect to sea ice type, incidence angle and frequency. Given these different findings in the literature, here in this study we assess within which range of incidence angles a newly formed sea ice classification can best be achieved.

2.2. Frequency effect on newly formed sea ice studies

The SAR frequency used also affects the results, as the sensitivity to the sea ice thickness is dependent on the penetration depth of the respective frequencies. L-band SAR has been shown to have a penetration depth up to tens of centimetres while the penetration depths into new sea ice for X- and C-band SAR are of the order of centimetres (Eriksson et al., 2010; Hallikainen and Winebrenner, 1992). As seen in Brekke et al. (2014) C-band SAR is more sensitive to sea ice with a thickness below 0.12 m and L-band SAR is more sensitive to sea ice thickness between 0.12 m and 0.36 m. Since the X-band frequency 9.6 GHz is higher than the C-band frequency (5.405 GHz) the X-band SAR will be even more sensitive to the thinner sea ice range.

The SAR frequency also affects the scattering processes values. Eriksson et al. (2010) observed that X-band SAR has slightly less volume scattering than C-band data, which is to be expected because the penetration depth is less. Following this and the deeper penetration we might expect the L-band SAR to have more volume scattering than the C-band data. Using C-band SAR, Carlström and Ulander (1995) and Dierking et al. (1999) showed that in the Baltic Sea for incidence angles below 45.8° and dry sea ice the HH channel is dominated by surface scattering.

3. Experimental setup and data collection

The Norwegian young sea ICE (N-ICE2015) campaign was carried out by the Norwegian Polar Institute and partners between January and June 2015. During the campaign R/V Lance was frozen into, and drifted with, the sea ice in the region north of Svalbard (Granskog et al., 2016). We use 59 high resolution (1–8 m) overlapping dual polarization X-band and quad-polarization C- and L- band SAR images obtained during this drift campaign. In addition, meteorological observations and accurate positioning data were collected on-board R/V Lance. In-situ data including helicopter-borne electromagnetic (EM) sea ice plus snow thickness measurements (King et al., 2016), ground based measurements of ice and snow thickness (Rösel et al., 2016) and salinity (Gerland et al., 2017), and sea ice drift (Itkin et al., 2015) were acquired in the study region north of Svalbard.

During this campaign newly formed sea ice was observed in previously open leads which had refrozen. We focus our study on these leads. The accuracy (± 0.10 m) (Haas et al., 2009) of the airborne EM thickness measurements means that while leads are easily identified within the thicker pack ice, it is not possible to differentiate between different classes of young ice in the leads based on the EM thickness alone. Therefore, we also make use of photographs taken and notes made during the helicopter flights to identify different classes of newly formed sea ice and surface structures. The newly formed sea ice classes observed during flights include thin ice with a thin snow cover, grey nilas as well as refrozen lead covered in frost flowers.

In this study, we make use of a six months long sequence of SAR data acquisition during which the air temperatures ranged from −31 °C to +1 °C. We investigate the effect of temperature and incidence angle on the newly formed sea ice observed within the SAR data. The three different frequencies, X-, C- and L-band, enable us to do comparative studies between the separate frequencies and their response to changes in temperature and incidence angle.

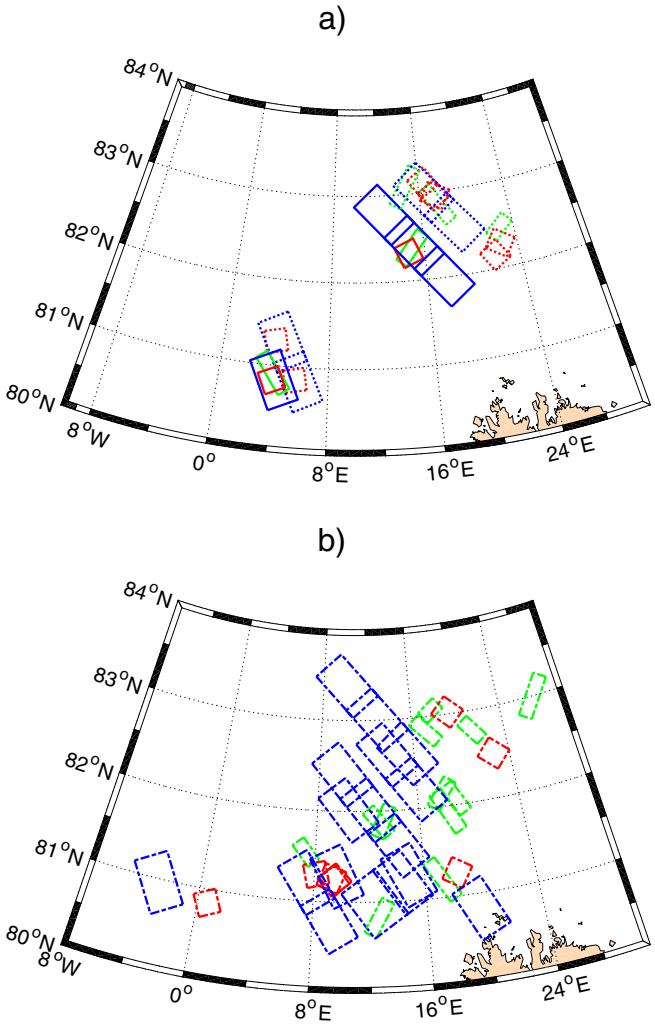

Fig. 1. Outline of the different satellite images used in the study, TerraSAR-X (green), RADARSAT-2 (red) and ALOS-2 (blue). a) Overlapping satellite scenes: Solid lines show satellite scenes that overlap in space and time with two other satellite scenes and dotted lines show scenes that overlap with one other scene. b) Non-overlapping satellite scenes with respect to time. (For interpretation of the references to colour in this figure legend, the reader is referred to the web version of this article.)

3.1. Study area

The study area is located north of Svalbard and extends from 7° W to 26° E and from 80° N to 84° N (Fig. 1). The study lasted from 12 January to 24 June 2015. R/V Lance was moored up to and drifted with four different sea ice floes (floes 1–4). When an ice floe that the ship was moored up to broke up, the ship was repositioned and moored up to a new ice floe further north-east (Granskog et al., 2016). The majority of the satellite images were obtained over or near the position of R/V Lance. The drifting pattern of the ship therefore affected the selected location of the satellite image acquisitions.

In-situ data from the N-ICE2015 drift ice study show that the ice cover primarily was a mixture of first-year ice and second-year ice (Granskog et al., 2017), though there were also areas with nilas, young grey ice and pancake ice. Frost flowers were often observed on top of the young ice during the entire N-ICE2015 drift study.

Table 1
Specifics of satellite data used in this study. The values presented are average values for the different missions. Specific values for the different satellite images are presented in Appendix A.

Mission	TerraSAR-X	RADARSAT-2	ALOS-2
Frequency band	X (9.65 GHz)	C (5.41 GHz)	L (1.2 GHz)
Acquisition mode	Stripmap	Polarimetric Fine	Stripmap Full Polarization
Polarization mode	Dual	Quad	Full (Quad)
Channels	HH/VV	HH/HV/VH/VV	HH/HV/VH/VV
Range (Rg) resolution*	1.2 m	5.2 m	5.1 m
Azimuth (Az) resolution *	4.8 m	7.6 m	4.3 m
Rg pixel spacing*	0.9 m	4.7 m	2.9 m
Az pixel spacing*	2.5 m	5.1 m	3.2 m
Width	16 km	25 km	40–50 km
Length (per frame)	55 km	25 km	70 km
Incidence angle range	20°–45°	18°–49°	29°–41°
Noise Equivalent sigma zero (NESZ)	−22.3 dB ± 1.4 dB	−32.9 db ± 1.5 dB	−36.0 dB (HH) −46.0 dB (HV)
*Nominal values			

3.2. SAR satellite data

During the N-ICE2015 drift campaign satellite images that overlapped in time and space were acquired. We use TerraSAR-X Stripmap dual polarization (HH/VV) (TerraSAR-X) images, RADARSAT-2 Fine Quad Polarization (RADARSAT-2) images and ALOS-2 Palsar-2 Stripmap Full Polarization (ALOS-2) images. Sensor details are given in Table 1 and Fig. 2 presents an example of semi-coincident SAR acquisitions of the three sensors. The SAR sensors on-board the different satellites operate at different frequencies, ranging from X- to L-band. A total of 17 TerraSAR-X images, 17 RADARSAT-2 as well as 25 ALOS-2 images were used in this study (Appendix A). Nine of the TerraSAR-X scenes were acquired in ascending mode and eight in descending mode. All but two RADARSAT-2 satellite images were acquired in ascending mode and all of the ALOS-2 satellite images. All data were acquired in single-look-complex (SLC) mode.

The TerraSAR-X and RADARSAT-2 scenes were obtained between January and June 2015 and the ALOS-2 scenes were obtained between April and June 2015. The time, incidence angle and middle swath noise floor (noise equivalent sigma zero (NESZ)) for the individual scenes are presented in Appendix A. In Table 1, the incidence angle range and the mean NESZ values are presented.

For two of the days, there is a set of satellite scenes for all three frequencies that overlap partly in space and time and for four days there is an overlap in space and time for two different frequencies (Fig. 1a). Aside from this, numerous individual satellite scenes that do not overlap in both space and time are used (Fig. 1b).

3.3. Airborne measurements

Airborne electromagnetic (AEM) soundings (Haas et al., 2009) were carried out from R/V Lance from 14 April 2015 to 18 May 2015 (Fig. 3 and Table 2). The AEM flights that overlap with satellite data and are utilised in this study are listed in Table 2 (King et al., 2016). Downward-looking photographs were taken with a GoPro camera (model YHDC5170) every 2 s. In this study, the photographs were used to extract visual information about the sea ice surface, e.g., snow cover, presence of frost flowers, rafting and sea ice type.

3.3.1. Airborne measurements data processing

The AEM system measures the distance to the sea water and the distance to the snow and ice surface and the difference between the two

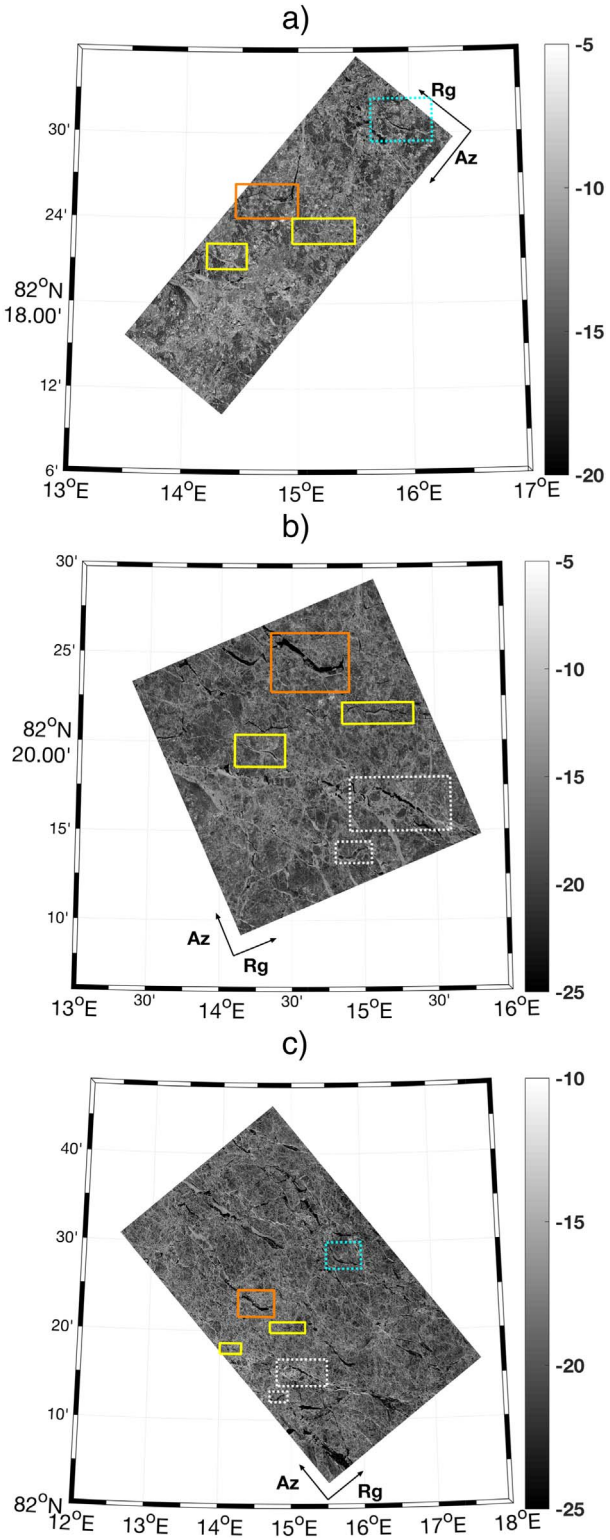

Fig. 2. Radar backscatter σ^0_{HH} scenes in dB from 28 April 2015 for a) TerraSAR-X, b) RADARSAT-2 and c) ALOS-2. The range (Rg) and azimuth (Az) directions are indicated with arrows. These scenes overlap in space and are separated by a few hours in time (see Appendix A). The scenes have different areal extent and hence do not completely overlap one-another (scenes B in Fig. 3). As references the orange and yellow boxes indicate the same areas in all three scenes and mark key features visible in all scenes. The dotted cyan box indicates an overlap between the X-band and the L-band scene. The white dotted boxes indicate an overlap between the C- and L-band scenes. (For interpretation of the references to colour in this figure legend, the reader is referred to the web version of this article.)

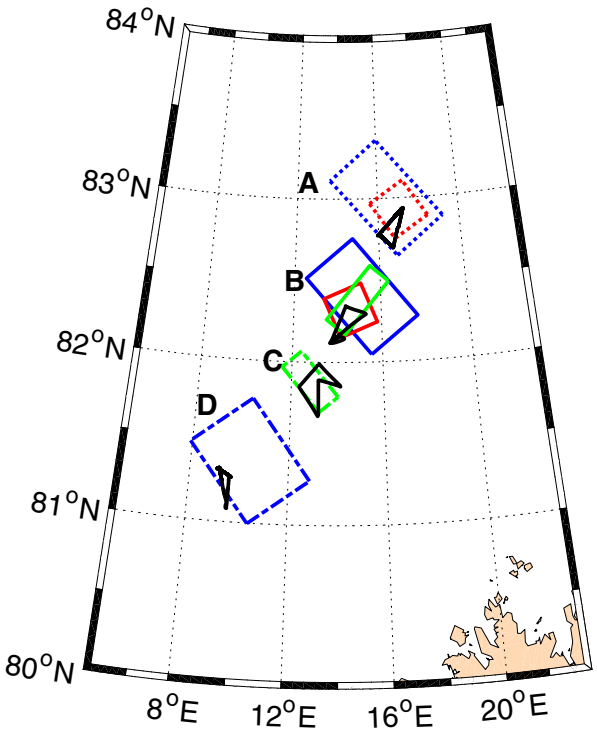

Fig. 3. Overlapping AEM flights (black), TerraSAR-X scenes (green), RADARSAT-2 scenes (red) and ALOS-2 scenes (blue). The letters A–D represents the respective AEM flights presented in Table 2. Solid lines show satellite scenes that overlap in space and time with two other satellite scenes and dotted lines show scenes that overlap with one other scene. Solitary scenes have a dashed outline. (For interpretation of the references to colour in this figure legend, the reader is referred to the web version of this article.)

Table 2
Outline of the AEM flights used in this study. For each of the flights the start time and stop time in UTC as well as the satellite data it is overlapping is presented. The # corresponds to the letters used in Fig. 3.

#	Date	Start time (UTC)	Stop time (UTC)	Overlapping SAR data
A	24 April 2015	14:24	15:27	C, L
B	29 April 2015	09:04	10:11	X, C, L
C	30 April 2015	09:10	10:15	X
D	18 May 2015	11:41	12:22	L

is the total ice and snow thickness, for details see Haas et al. (2009). The nominal uncertainty for a single measurement is 0.10 m for level ice, with significantly larger errors occurring in heavily ridged areas (Haas et al., 2009). The footprint of the AEM system is approximately 40 × 40 m, with point spacing of measurements approximately 4 m.

3.3.2. Time separation correction

The sea ice drift displacement between the different satellite scenes and the AEM flights was corrected for by using the drift track from R/V Lance. The AEM measurements were relocated to the overlapping satellite image acquisition time assuming a uniform average sea ice drift velocity within the region. This method does not account for rotation of the ice within the region, or for local variations in drift speed. Therefore, following the initial relocation of the AEM measurements, the position was manually adjusted into the best possible match with the image, using obvious leads within the flight path and image. For flights #A, B and D, the data was drift corrected to the time of the ALOS-2 scene closest in time (Appendix A) and for flight #C the data was displaced to overlap with the TerraSAR-X scene closest in time (Appendix A).

3.4. Environmental conditions

Air temperature at 2 m a.s.l. and wind speed at 10 m a.s.l. were recorded by instruments mounted on a 10-m-tall meteorological tower situated on the sea ice 300 to 400 m away from the research vessel (Hudson et al., 2015). The air temperatures were measured with a Vaisala HMP155 (RM Young Model 43502) and the wind speed with a Lufft Ventus V200A-UMB. The data was recorded every second and averaged over one minute. In addition, air temperature and wind speed measured at 22 m a.s.l. on-board R/V Lance every 30 s and averaged over 1 min. The weather station on-board R/V Lance used an Aanderaa air temperature sensor (model number 3455) and a Thies Clima 2D ultrasonic wind sensor. The primary weather measurements are the ones measured on the sea ice and gaps in the data were replaced with weather data from the ship based sensors, for details see Cohen et al. (2017) and Hudson et al. (2015). The mean difference between the ice based and ship based temperature sensors was small (0.18 °C with a standard deviation of 0.85 °C; Hudson et al., 2015). The gaps in the on-ice weather data primarily relate to the time from when R/V Lance moored up to a new floe and before the meteorological tower could be installed, and when the meteorological tower had been dissembled before the ship left a floe. The sea ice based meteorological measurements are shown in black in Fig. 4 and the ship based measurements are show in magenta.

4. Methodology

4.1. SAR satellite data processing

For consistency, all satellite scenes were pre-processed in the same way. Firstly, the scenes were radiometrically calibrated to complex backscatter values using the included metadata calibration information, see Airbus Defence & Space (2014) (X-band), MacDonald, Dettwiler and Associates Ltd. (2016b) (C-band), and Shimada et al. (2009) (L-band). Secondly, the satellite images were multi-looked (Oliver and Quegan, 2004) to reduce image speckle. The amount of multi-looking was selected so that the different images would have similar pixel size. Since the individual scenes with a given frequency have different pixel size (Table 1) the multi-looking is different for each scene. The multi-looked ground range pixel size was set to correspond to the AEM footprint, i.e., approximately 40 × 40 m. This means that the TerraSAR-X scenes were processed with on average 25 × 16 looks (range vs azimuth), the RADARSAT-2 images with on average 7 × 5 looks and the ALOS-2 with on average 7 × 12 looks. The satellite images were geocoded to a Polar Stereographic coordinate system using the WGS84 ellipsoid.

4.2. Newly formed sea ice mask

The satellite images were segmented using the algorithm presented in Doulgeris and Eltoft (2010) and Doulgeris (2013). The segmentation algorithm aims to separate the image into different regions based on the statistical properties of the data. The same segmentation algorithm was used for the three types of satellite images but note that for the TerraSAR-X images we only have two co-polarization bands. Variations in incidence angles are not accounted for in the algorithm. As the incidence angle variations within each satellite scene are of the order of a few degrees it is assumed to have a negligible effect.

Once the scenes were segmented, areas with newly formed sea ice were identified visually. The SNR is not taken into account though were not observed to produce any effects that could not be addressed at the visual identification stage. Examples of segmented SAR images based on the same approach as here are given in, e.g., Johansson et al. (2017) and Moen et al. (2015, 2013). Sea ice observations from R/V Lance, AEM flight information as well as meteorological data were used to aid this identification.

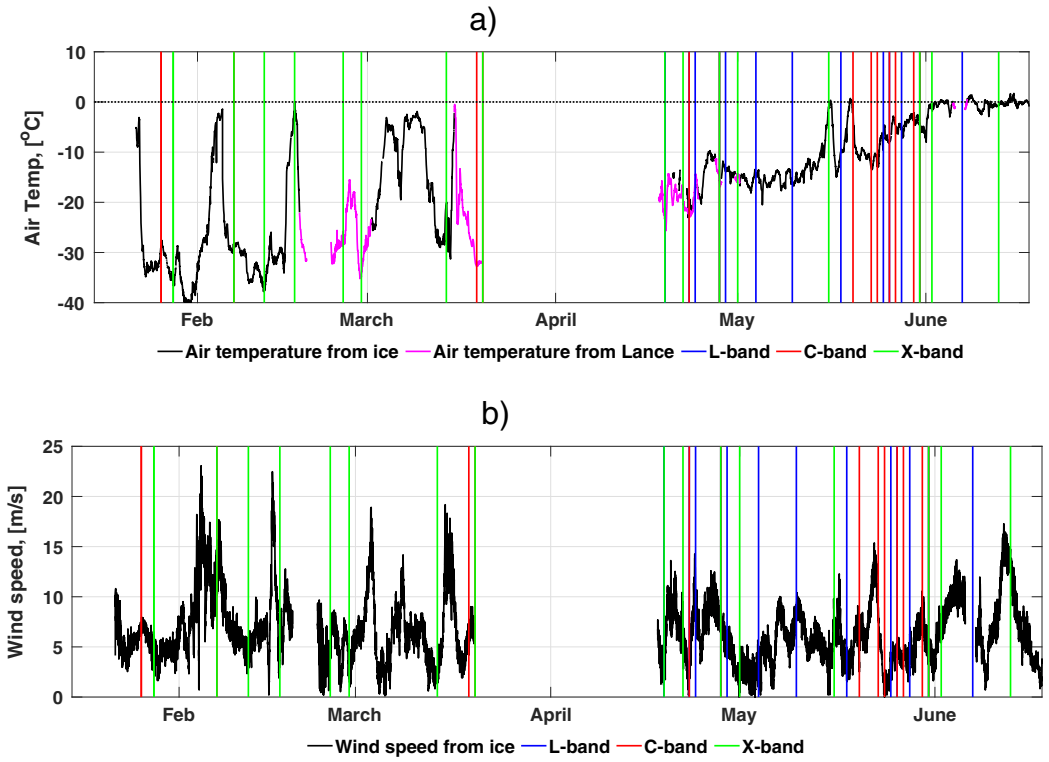

Fig. 4. Meteorological data. a) Air temperature. b) Wind speed. The black lines indicate the data measured on the sea ice and the magenta lines indicate data measured on-board R/V Lance. The vertical lines indicate time of satellite image acquisitions for X-band (green), C-band (red), and L-band (blue). The dotted black line in a) marks 0 °C. The lack of data from the end of March until mid-April corresponds to the mid-way break in the drift ice study. (For interpretation of the references to colour in this figure legend, the reader is referred to the web version of this article.)

In the following, we only analyse SAR data from these identified areas with newly formed sea ice.

4.3. Polarimetric characteristics of sea ice

Within this study, we analyse the newly formed sea ice polarimetric SAR information for various incidence angles, SAR frequencies and temperatures. We compare how the newly formed sea ice in leads is observed using the (i) co-polarization ratio, (ii) polarization difference, (iii) scattering entropy, and (iv) scattering angle.

4.3.1. Polarimetric information

The full scattering matrix **S**, is defined as;

$$\boldsymbol{S} = \begin{bmatrix} S_{HH} & S_{VH} \\ S_{HV} & S_{VV} \end{bmatrix} = \begin{bmatrix} |S_{HH}|e^{j\phi_{HH}} & |S_{VH}|e^{j\phi_{VH}} \\ |S_{HV}|e^{j\phi_{HV}} & |S_{VV}|e^{j\phi_{VV}} \end{bmatrix}. \quad (1)$$

The first letter in the subscript refers to the transmitted polarization and the second the received polarization. $|\cdot|$ and ϕ denote the amplitudes and the phases of the measured complex scattering coefficients. We assume reciprocity, i.e., $S_{HV} = S_{VH}$.

4.3.2. Feature definitions

The data was calibrated so that the pixel values could be directly related to the radar backscatter coefficient (σ^0) values. The backscattering coefficients in dB are given as;

$$\begin{aligned} \sigma^0_{HH} &= 10 \times \log_{10}(\langle |S_{HH}|^2 \rangle), \\ \sigma^0_{HV} &= 10 \times \log_{10}(\langle |S_{HV}|^2 \rangle), \quad and \\ \sigma^0_{VV} &= 10 \times \log_{10}(\langle |S_{VV}|^2 \rangle), \end{aligned} \quad (2)$$

where $\langle \cdot \rangle$ is averaging over a neighbourhood of N pixels. Hence, Eq. (2) represents the multi-looked intensity images for the three polarization channels.

For the feature analysis, the co-polarization ratio (γ_{co}) was calculated as;

$$\gamma_{co} = 10 \times \log_{10}\left(\frac{\langle |S_{VV}|^2 \rangle}{\langle |S_{HH}|^2 \rangle}\right). \quad (3)$$

Assuming that we are within the Bragg domain the ratio is independent of roughness, but dependent on the complex relative permittivity of the medium and the incidence angle (θ).

The polarization difference (PD) was calculated as;

$$PD = \langle |S_{VV}|^2 \rangle - \langle |S_{HH}|^2 \rangle. \quad (4)$$

Note that PD is defined on a linear scale and may suppress non-polarized scattering (Kudryavtsev et al., 2013). Kudryavtsev et al. (2013) successfully used PD to enhance the signature of near-surface wind variability and presence of oil spills in open water. Oil spills are generally characterised by low backscatter values (Brekke et al., 2014) and as such have a comparable polarimetric response to the newly formed sea ice areas discussed here. Using PD the non-polarized component can be separated from the polarized one in the analysed data.

The scattering entropy (H) is one part of the H/α decomposition by Cloude and Pottier (1997), where α is the scattering angle. In this study the SAR classification scheme of Cloude and Pottier (1997) is used to distinguish between the different types of scattering mechanisms for the fully polarimetric RADARSAT-2 and ALOS-2 images. For the TerraSAR-X scenes, a dual-polarization H/α decomposition is made.

For the H/α decomposition we first define the Pauli scattering vector **k** for quad-polarization data;

$$\boldsymbol{k} = \frac{1}{\sqrt{2}}[S_{HH} + S_{VV} \quad S_{HH} - S_{VV} \quad 2S_{HV}]^t \quad (5)$$

where t denotes the vector transpose. For dual-polarization (HH/VV) data the scattering vector becomes;

$$\boldsymbol{k} = \frac{1}{\sqrt{2}}[S_{HH} + S_{VV} \quad S_{HH} - S_{VV}]^t. \tag{6}$$

The H/α decomposition parameters are then calculated from the eigenvalues and eigenvectors of the coherency matrix $\mathbf{T}_d$. The $d \times d$ coherency matrix $\mathbf{T}_d$ is defined as;

$$\boldsymbol{T}_d = \frac{1}{L}\sum_{j=1}^{L} \mathbf{k}_j \mathbf{k}_j^{*t} \tag{7}$$

where d is the polarimetric dimension, i.e., for the dual-polarization data $d = 2$ and for the quad-polarization data $d = 3$. $\mathbf{k}_j$ is the single-look complex measurement corresponding to pixel number j. The superscripts * denote the complex conjugate, and L is the number of samples

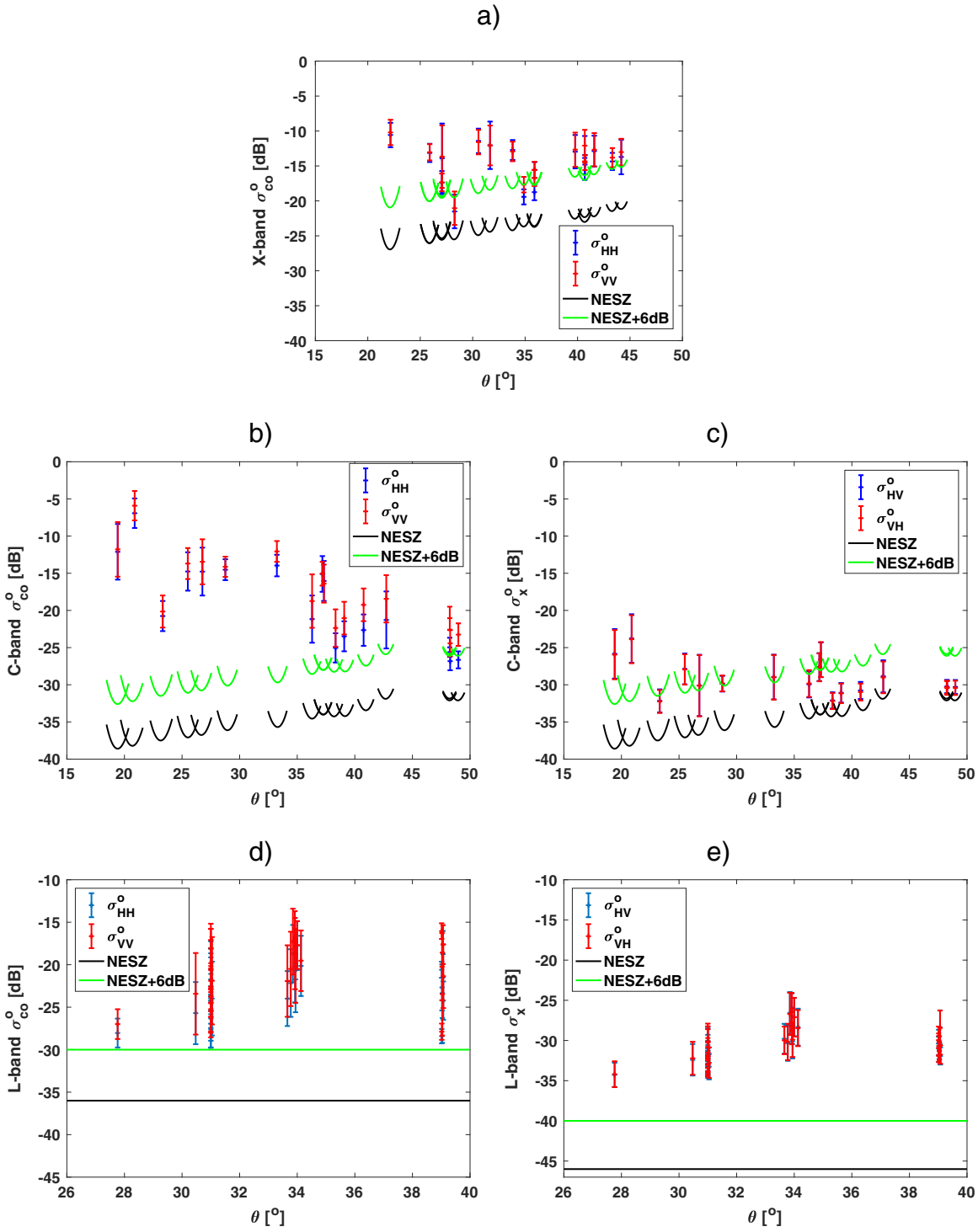

Fig. 5. Signal-to-noise analysis for the newly formed sea ice areas in a) X-band σ^0_{co}, b) C-band σ^0_{co}, c) C-band σ^0_x, d) L-band σ^0_{co} and e) L-band σ^0_x. The blue bars indicate mean and standard deviation of σ^0_{HH} in a), b) and d) and mean and standard deviation of σ^0_{HV} in c) and e). The red bars indicate the mean and standard deviation of σ^0_{VV} in a), b) and d) and the mean and standard deviation of σ^0_{VH} in c) and e). The black lines in a)–c) represent the NESZ for each individual scene and in d) and e) the standard NESZ for L-band. The green lines in a)–e) are 6 dB above the NESZ. The incidence angle corresponding to each scene is the centre incidence angle. (For interpretation of the references to colour in this figure legend, the reader is referred to the web version of this article.)

included in the computation of the coherency matrix.

H is a measure of the randomness of the scattering process and takes values between 0 and 1. In the limiting case of $H = 0$, only one type of scattering mechanisms dominates while H approaching 1 indicates a depolarized signal. α can be used to identify dominant scattering mechanisms. Values below 42.5° are indicative of surface scattering, values between 42.5° and 47.5° represent volume scattering and values between 47.5° and 90° are evidence of double-bouncing scattering (Lee and Pottier, 2009). The scattering entropy was calculated as;

$$H = -\sum_{i=1}^{d} p_i log_d p_i \tag{8}$$

where d is the polarimetric dimension, i.e., $d = 2$ for the dual-polarization data and $d = 3$ for the quad-polarization data. λ_i are the polarimetric eigenvalues of $\mathbf{T}_d$ and $p_i = \lambda_i/(\lambda_1 + \lambda_2 + \lambda_3)$ for the quad-polarization calculations and $p_i = \lambda_i/(\lambda_1 + \lambda_2)$ for the dual-polarization calculations.

The mean scattering angle (α) was calculated as;

$$\alpha = \sum_{i=1}^{d} p_i \alpha_i \tag{9}$$

where $\alpha_i = \cos^{-1}(|\mathbf{e}_i(1)|)$ is the scattering angle corresponding to the ith eigenvector $\mathbf{e}_i$ (Cloude and Pottier, 1997).

For the scattering entropy calculations, we use the full polarimetry data in the case of RADARSAT-2 and ALOS-2. For TerraSAR-X, the HH and VV channels are used for the entropy calculations. These results are therefore not directly comparable with the fully polarimetric entropy calculations. In order to facilitate a direct comparison, for overlapping satellite scenes the RADARSAT-2 and ALOS-2 scenes are converted to dual-polarization data (HH and VV) and a dual-polarization scattering entropy calculation is performed.

4.4. Noise analysis

Newly formed sea ice often dampens the surface waves and hence reduces the backscatter signal. Undisturbed thin ice regions (< 0.10 m) are generally characterised by below average backscatter values across the C- and L-band scenes. Wakabayashi et al. (2004) observe high backscatter values across the X-band scenes. In this study, however, we also observed below average backscatter for the X-band scenes over the newly formed sea ice areas. In all these cases, the reduced backscatter signal may then approach the sensor noise floor, i.e., reducing the SNR levels. In our case, the X-band data has a higher sensor noise floor and the data within these scenes may therefore be more affected by noise when the backscatter signal is reduced.

The backscatter values of the cross-polarization channels (σ_x^0), i.e., the σ_{HV}^0 and σ_{VH}^0 channels, are known to be lower than the corresponding co-polarization channels (σ_{co}^0), i.e., the σ_{HH}^0 and σ_{VV}^0 channels, over open water and newly formed sea ice. These cross-polarization channel values therefore often have lower SNR than the co-polarization channel values.

Thermal noise that influences the backscatter values is known to raise the H and α values (Kudryavtsev et al., 2013; Skrunes et al., 2015). Hence, when analysing the low backscatter newly formed sea ice areas it is important to include the noise floor in the analysis.

The NESZ values for the TerraSAR-X and RADARSAT-2 scenes are calculated using specified meta data information as well as the local incidence angle. Details on the NESZ calibration for TerraSAR-X are found in Airbus Defence & Space (2014). The NESZ values for the RADARSAT-2 scenes are beam specific values, (MacDonald, Dettwiler and Associates Ltd., 2016a). For ALOS-2, the NESZ is a sensor specific value and does not vary with incidence angle or scene (Shimada et al., 2015), but one values is given for the HH channel and one for the HV channel. The NESZ must be lower than the measured normalised radar cross section in order for the signal not to be affected by the noise and potentially be at least 6 dB above the noise floor to safely contain a valid signal (Freeman and Durden, 1998; Minchew et al., 2012). The sigma nought backscatter values for the segmented newly formed sea ice areas are therefore compared to the scene specific NESZ values (Fig. 5). The 6 dB level is not a well quantified value and we have therefore chosen to use 2 dB increments above the NESZ values in the presentation of our results to further investigate the impact of the noise floor.

For the L-band scenes the σ_{co}^0 and σ_x^0 have values 6 dB or more above the noise floor. For C-band, for $\theta > 23°$, the σ_x^0 values are in part within the 6 dB margin of the noise floor. For $\theta > 47°$, also the σ_{co}^0 can be below the 6 dB range but always stays above the noise floor. We therefore use all C- and L-band co-polarization data and for L-band also all cross-polarization data. For C-band, only the cross-polarization data at low incidence angles is high enough above the noise floor to include all polarization data. For X-band, more care has to be taken, as for many scenes the co-polarization values of the leads can be below the NESZ + 6 dB safety margin.

5. Multi-sensor analysis

In the following section, we present polarimetric values for newly formed sea ice for three different frequency data sets. The scenes contain a range of incidence angles and were acquired under different environmental conditions. A comparative study of the polarimetric response with respect to the effect of incidence angle and temperature is therefore possible.

5.1. Characteristics of newly formed sea ice

Newly formed sea ice was observed throughout the N-ICE2015 drift study. The percentage of newly formed sea ice within each scene varied during the campaign and between the different frequency data sets (Johansson et al., 2016). On average the newly formed sea ice made up 9.6% of the X-band scenes, 4.8% of the C-band scenes and 10.7% of the L-band scenes according to our classification (see Section 4.2). The larger penetration depth in L-band compared to X- and C-band means that the newly formed sea ice that is identified and separated from the surrounding areas in L-band data can be slightly thicker. Within spatially overlapping C- and L-band scenes, Johansson et al. (2016) were able to identify a higher proportion of leads within the L-band scenes. Newly formed sea ice with frost flowers on the surface is often misclassified due to the high roughness and volume scattering introduced by the frost flowers (Isleifson et al., 2014; Martin et al., 1995). However, they can be easier identified within the L-band scenes compared to the X- and C-band scenes, as the L-band frequency is less sensitive to such surface structures (Arkett et al., 2008; Dierking and Busche, 2006). In summary, the combination of high penetration depth, high spatial resolution, and lower sensitivity to frost flowers could make it easier to separate newly formed sea ice from the surrounding sea ice and open water in L-band SAR than for X- and C-band SAR at the same pixel spacing. In our case, however, the high spatial resolution of the X-band scenes before the multi-looking improves the separation of the thin structures within the segmentation, and thus promotes a higher likelihood of correctly identifying leads, specifically narrow leads, as already observed in Eriksson et al. (2010). We can therefore expect to identify a higher proportion of small scale structures, such as leads, within the X-band scenes compared to C-band scenes. In the following we will test these hypothesis with our large SAR data set.

In Fig. 6, γ_{co} and H values for newly formed sea ice areas as well as other, thicker ice classes and open water are presented. The segmentation of surface types is based on the method presented in Section 4.2 and a manual labelling of the different surface classes. The figure is made up of data from one scene for each frequency data set with similar incidence angles but not overlapping the same area and not acquired at the same time. The θ value for X-band is 40.7°, for the C-band scene

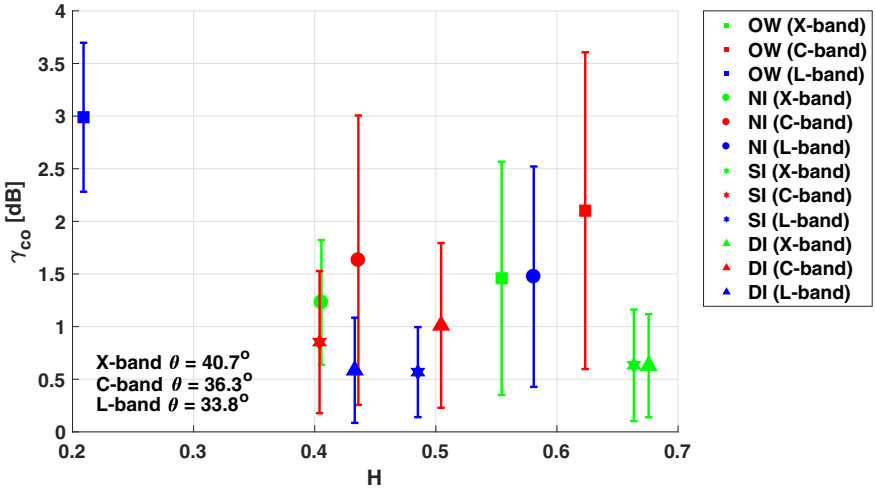

Fig. 6. γ_{co} versus H values for open water (OW), newly formed sea ice (NI), smooth sea ice (SI), and deformed sea ice (DI) for the three different frequencies. The markers indicate the mean values and the error bars indicate ± one standard deviation (std). The same markers are used for the different frequencies, though X-band is plotted using green, C-band using red and L-band using blue markers. The X-band scene was acquired at 7 February 2015, the C-band scene on 20 March 2015 and the L-band scene on 23 April 2015. (For interpretation of the references to colour in this figure legend, the reader is referred to the web version of this article.)

36.3° and for the L-band scene 33.8°. The surface temperatures at the times of the satellite scenes were all below −20 °C. The newly formed sea ice (NI) areas are possible to separate from the thicker and older ice classes, smooth sea ice (SI) and the deformed sea ice (DI) areas, as well as from the open water (OW) areas for all the frequencies (Fig. 6).

A subsection of the L-band scene from 23 April 2015 (Fig. 6) is shown in Fig. 7d. The open water areas with below average H values compared to the rest of the scene are easily detected as dark blue areas. The NI areas have *H* values higher than for the surrounding sea ice areas and they are also easily distinguished within the L-band scene and to some extent within the C-band scene (Fig. 7a and d). The lead annotated *Lead 1* shows two distinctly different zones of *H* values for the eastern and western part of the lead. Photographs show that the westernmost half of the lead was made up of newly formed sea ice with small scale surface structures (Fig. 7I) and it had a mean snow and ice thickness of 0.3 m according to the AEM measurements. The easternmost half of the lead was made up of one smooth newly formed sea ice section (Fig. 7II) with a mean snow and ice thickness of 0.23 m. Photographs show that the entire lead is covered in frost flowers. In the L-band scene the smooth part of the lead (II) has the highest *H* and α (Fig. 1 supplementary information) values and for the C-band scene the opposite is true. For the L-band scene the H/α values for the smooth part II are within the domain of the dipole type scattering mechanisms (Cloude and Pottier, 1997) and for part I within the surface scattering domain. The scattering values within part II of the lead could be a consequence of the penetration depth for L-band SAR, where the scattering is expected to be a result of the ice-water boundary (Wakabayashi et al., 2004). Part I of the lead likely experiences more surface scattering due to the rougher surface and rafting of the ice as seen in the aerial photographs. For the C-band scene, the entire lead is within the surface scattering domain (Cloude and Pottier, 1997). The rougher surface part of the lead (I), however, has higher scattering entropy values than the smoother part (II), which is opposite to L-band.

Lead 1 is one of a few within this study where the γ_{co} values are negative (not shown). In total, four of the X-band scenes and the C-band scene from 23 April 2015 have leads with negative γ_{co} values. Not all the leads within these scenes had negative γ_{co} values. The magnitude of the γ_{co} values is comparable regardless of whether they are positive or negative. In this study, we present mean γ_{co} values and we therefore consider the absolute values of the γ_{co} on a logarithmic scale from Section 5.2 and onwards. Geldsetzer and Yackel (2009) argue that the second-order volume scattering caused by brine-wetted snow cover may be a reason for negative γ_{co} values in the C-band data. However, while there was a significant amount of snow during the N-ICE2015 campaign (Granskog et al., 2017) brine wetted snow was not directly observed.

In Fig. 8, a similar lead is shown in a subsection of the X-band scene from 1 May 2015. The lead crosses from east to west in the lower part of the X-band scene. The AEM snow and ice thickness measurements show that the northernmost part of the lead, denoted as I in Fig. 8a, has a mean snow and ice thickness of 0.3 m. This part of the lead consists of young grey and young white ice with a light snow cover and evidence of some finger rafting (Fig. 8I). The middle of the lead, the dark area denoted II, is confirmed by the photographs to be young grey ice and nilas with frost flowers (Fig. 8II). The light area denoted III in Fig. 8a, is made up of snow covered young grey ice with some thicker floes and has a mean snow and ice thickness of 0.76 m (Fig. 8III). This latter measured thickness is likely to be an overestimate due to a mixture of thicker ice floes and younger grey ice within the footprint of the AEM instrument. The thinnest newly formed sea ice was observed in the area denoted II, and this area corresponded to the highest X-band γ_{co} values (Fig. 8b), which very well separates this thin ice area from all other ice classes. The low SNR is apparent in Fig. 8c where the area denoted II have a low SNR and a corresponding high scattering entropy.

The variations in thickness and surface roughness that are characteristic of refrozen leads strongly affect the backscatter signature. In Fig. 9, a close up of the lead observed within the orange box in Fig. 2 on the 28 April 2015 is shown. We can observe a few common trends, e.g., the γ_{co}, α and *PD* values increase over the newly formed sea ice areas for C- and L-band. However, this increase is not uniform over the lead and indicates that additional information about ice type and thickness is included. The *H* values vary over the lead ice, though a change in magnitude compared to the surrounding thicker ice is always observed. The photographs from the AEM flight on 29 April 2015 (#B Table 2) show a mixture of pancake ice and very thin ice within the leads.

5.2. *Effect of incidence angle on the co-polarization ratio and the polarimetric difference*

To study whether the incidence angle has to be taken into account for newly formed sea ice monitoring at different frequencies we here study the dependence of $|\gamma_{co}|$ and *PD* on the incidence angle. An incidence angle dependence is observed for the $|\gamma_{co}|$ values derived from the C-band scenes (Fig. 10). The Pearson's correlation between $|\gamma_{co}|$ and θ is 0.82. This dependence is not present or much less pronounced within the X- and L-band scenes. The Pearson's correlations are 0.29 and 0.34 respectively. It should be noted that the L-band scenes have, in comparison to the other two frequencies, a more limited range of incidence angles. The colouration of the different bars within Fig. 10 is based on the distance between the mean σ^0_{HH} values and the NESZ. We can observe that within the C-band data the higher $|\gamma_{co}|$ values are from backscatter data that is closer to the noise floor and are derived from

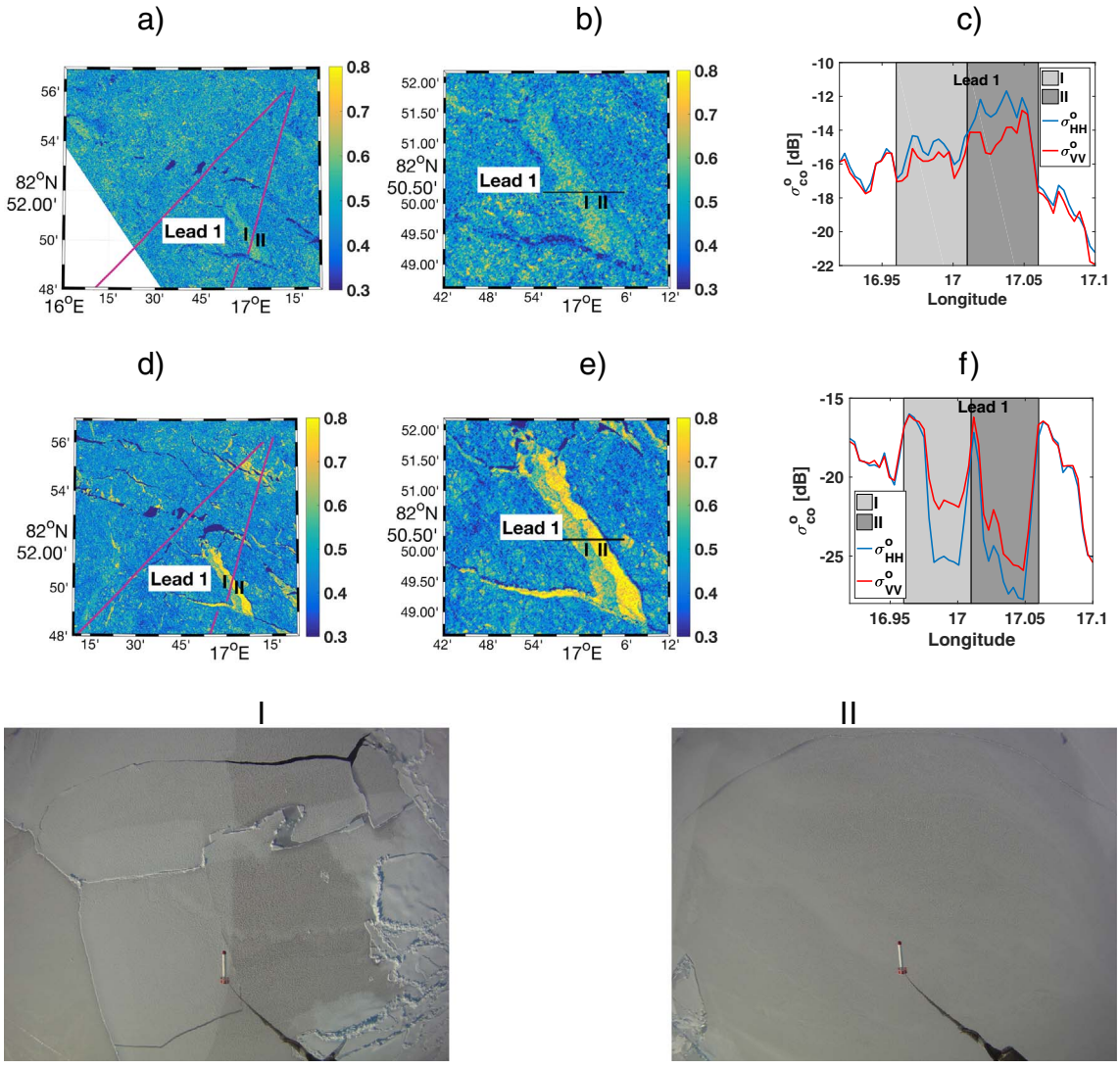

Fig. 7. Scattering entropy H on 23 April 2015 in a) C-band and d) L-band. θ for the C-band scene is 37.3° and for the L-band scene is 33.8°. The purple line is the AEM flight line from #A in Table 2. The break in the flight line is due to calibration measurements conducted in mid-flight. b) and e) are close-ups of a) and d) respectively. c) and f) are σ^0_{co} values from the black transect line in b) and e). The lighter grey shaded area represents the part of the lead denoted I and the darker grey shaded area the part of the lead denoted II. Panels I–II are photographs taken along the flight line. The photographs are taken in the middle of the westernmost part (I) of the lead denoted as *Leads 1* and II are taken in the middle of the easternmost part of *Lead 1*. The photographs covers a surface area of approximately 40 m × 40 m. (For interpretation of the references to colour in this figure legend, the reader is referred to the web version of this article.)

scenes with higher incidence angles.

The dependence of $|\gamma_{co}|$ on the incidence angle for C-band found here corresponds well with the finding of other studies (Fig. 11), where higher incidence angles also were found to correspond to higher $|\gamma_{co}|$ values. None of the other studies covered the same wide incidence angle range as this study but combined they show a $|\gamma_{co}|$ dependence with incidence angle similar to the one we observe here.

For X- and L-band data, there is limited information in the literature about the γ_{co} values for newly formed sea ice. One study by Nakamura et al. (2005) used an incidence angle of 45° and found γ_{co} values of 2 dB for X-band and 2.1 dB for L-band. The incidence angle used in their study is within the upper range of incidence angles used here, but the values are comparable (Fig. 10).

Comparing the linear difference between the VV and the HH channel values, i.e., the *PD*, we observe no incidence angle dependence (Fig. 12). The standard deviation is larger for the C-band scenes compared to the other frequency data sets. The smaller the SNR the smaller the standard deviation. Comparing the *PD* values to the σ^0_{VV} values we observe that the higher the σ^0_{VV} values, the higher the *PD* values (not shown).

In summary, we observe that for an operational automatic method to detect thin ice using C-band SAR the incidence angle dependence on the $|\gamma_{co}|$ values needs to be taken into account. Due to the closeness to the noise floor at higher incidence angles, low to medium incidence angles may be preferable for newly formed sea ice detection. The problem is much less pronounced for X- and L-band SAR and for that reason these frequencies may be a useful complement to C-band SAR. However, at present no satellite acquires these frequencies with the temporal and spatial regularity required for an operational service, e.g., similar to the C-band acquisitions done by Sentinel-1 and by RADARSAT-2 for the Canadian Ice Service. *PD* is less affected by the incidence angle and may therefore be a useful complement to the $|\gamma_{co}|$ values for all three frequencies.

5.3. *Effect of incidence angle on the scattering entropy and α values*

Similar to the dependence of the $|\gamma_{co}|$ on incidence angle (previous section) we here investigate the effect of incidence angle on the scattering entropy H and α. If the influence is strong these values cannot universally be used to detect newly formed sea ice. The incidence angle

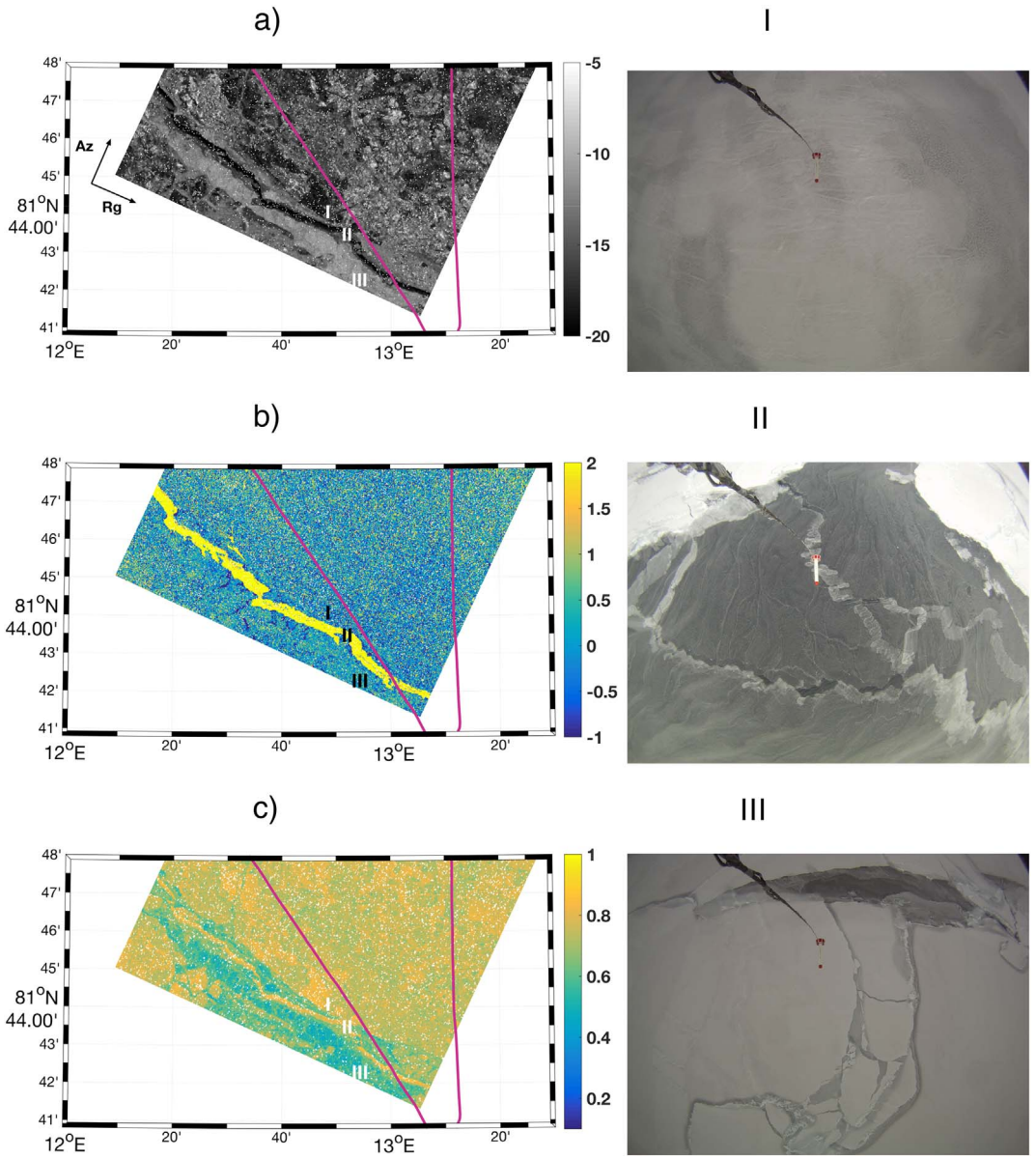

Fig. 8. Subset of an X-band scene from 1 May 2015. a) σ^0_{HH} in dB, b) γ_{co} in dB, and c) Scattering entropy H. The purple lines indicate the flight track from the AEM #C in Table 2. Panels I-III are photographs (surface area 40 m × 40 m) taken along the flight line and they roughly corresponding to the I-III notations within a)–c). (For interpretation of the references to colour in this figure legend, the reader is referred to the web version of this article.)

will then have to be accounted for in newly formed sea ice studies.

As the X-band scenes only contain the co-polarization channels the overlapping C- and L-band scenes have been reduced to the same bands for a comparison of the H and α values over the newly formed sea ice areas. The quad-polarimetry α values differ substantially from the dual-polarimetry α values for both the C- and L-band data and hence a direct comparison between all three frequencies with regards to α values is therefore not possible. The trend between the H and the α values is similar in the C- and L-band quad-polarimetric scenes, where an increase in H correspond to an increase in α. A majority of the C- and L-band data fall within the surface scattering regime, i.e., have $\alpha < 42.5°$, though the α values are higher for the L-band scenes than for the C-band scenes.

The quad-polarimetric and dual-polarimetric H values have a Pearson's correlation of 0.99 for the L-band scenes and of 0.90–0.98 for the C-band scenes. Given the high correlation a direct comparison between the dual-polarization and the quad-polarization H values is possible. This implies that dual-polarization X-band data can be used to complement the other frequencies. Moreover, since the co-polarization channels have higher backscatter values and higher SNR values than the cross-polarization channels the distance to the noise floor is increased by the reduction in dimensionality. Dual-polarization (HH + VV) scattering entropy values may therefore be a useful addition to newly formed sea ice identification, monitoring, and separation.

In Fig. 13, the H values are plotted versus the incidence angle. The highest H values in the C-band scenes relate to the highest incidence angles and the smallest range above the NESZ. The Pearson's correlation between H and θ is 0.83 for C-band. A similar incidence angle dependence is noted for the X-band data with a Pearson's correlation of 0.56. One high entropy outlier is observed when the σ^0_{HH} value is closest to the NESZ values (blue colour in Fig. 13a). No such incidence angle dependence can be observed for the L-band data, though a limited range of incidence angles are used in this study. Wakabayashi et al. (2004) observed an incidence angle dependence for the scattering entropy for L-band SAR, similar to the one observed here for X- and C-band SAR. We, however, cannot confirm this from the cases observed in this study.

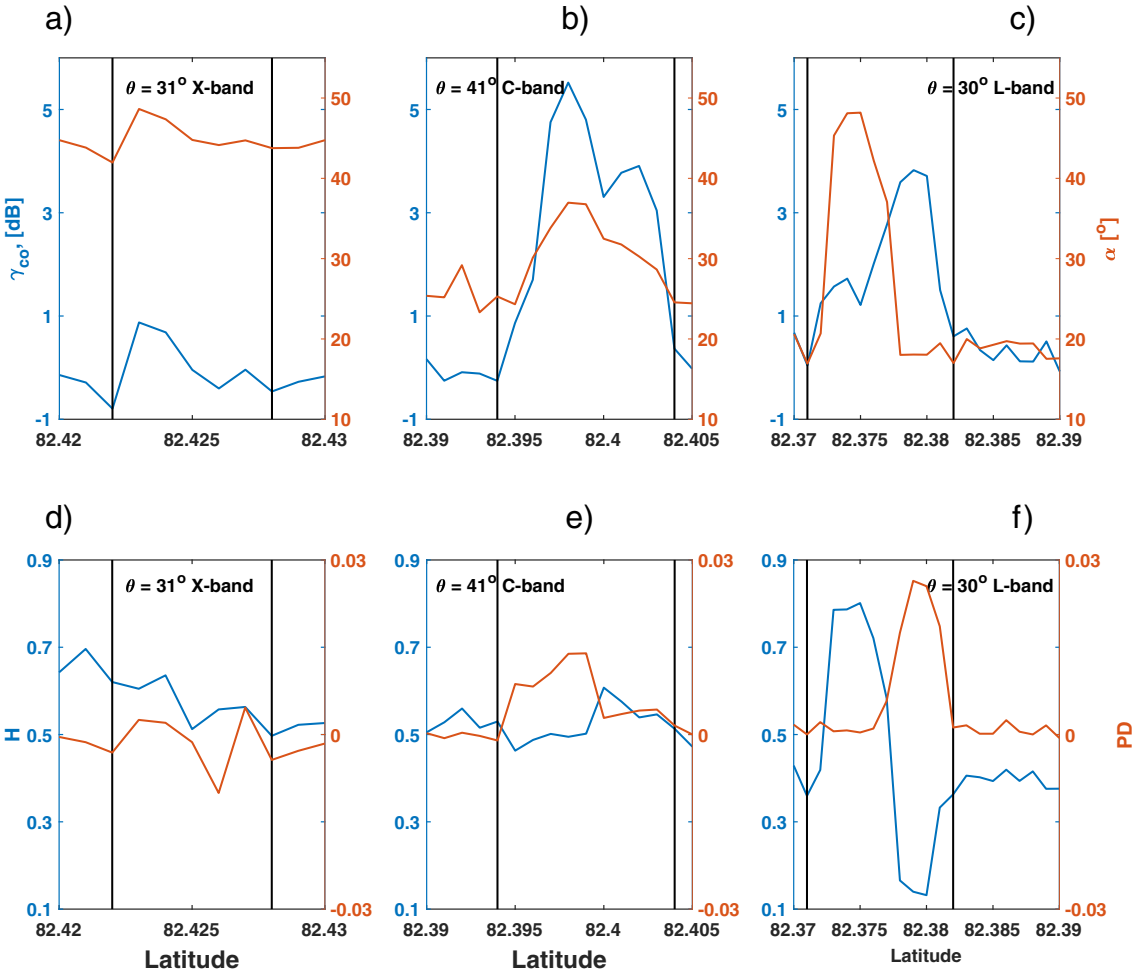

Fig. 9. Close-up of one lead from 28 April 2015 (orange box in Fig. 2). γ_{co} is plotted in blue together with α in orange for (a–c) and H (blue) are plotted together with PD (orange) for (d–f). X-band data is presented in the left column, C-band in the middle, and L-band in the right column. The black vertical lines indicate the start and the end of the lead. Sea ice drift between the time of acquisitions of the satellite scenes means that a shift in location has occurred between the different scenes. (For interpretation of the references to colour in this figure legend, the reader is referred to the web version of this article.)

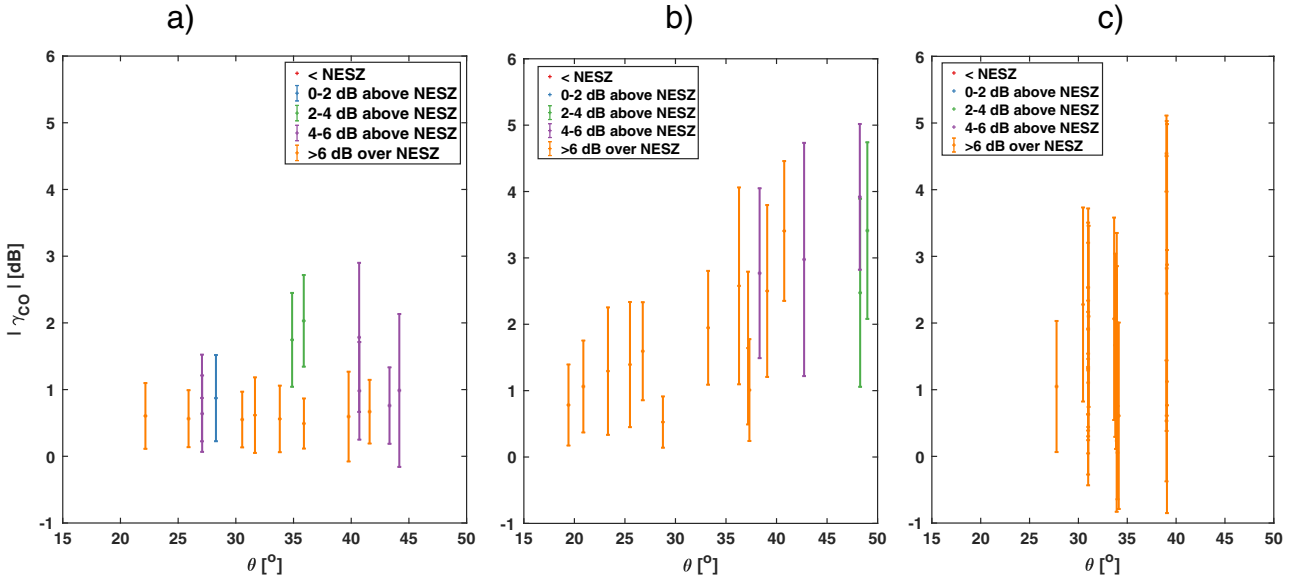

Fig. 10. $|\gamma_{co}|$ values versus the incidence angle for a) X-band, b) C-band and c) L-band. The colours on the lines corresponds to the mean σ^0_{HH} minus one std above the NESZ for each scene. (For interpretation of the references to colour in this figure legend, the reader is referred to the web version of this article.)

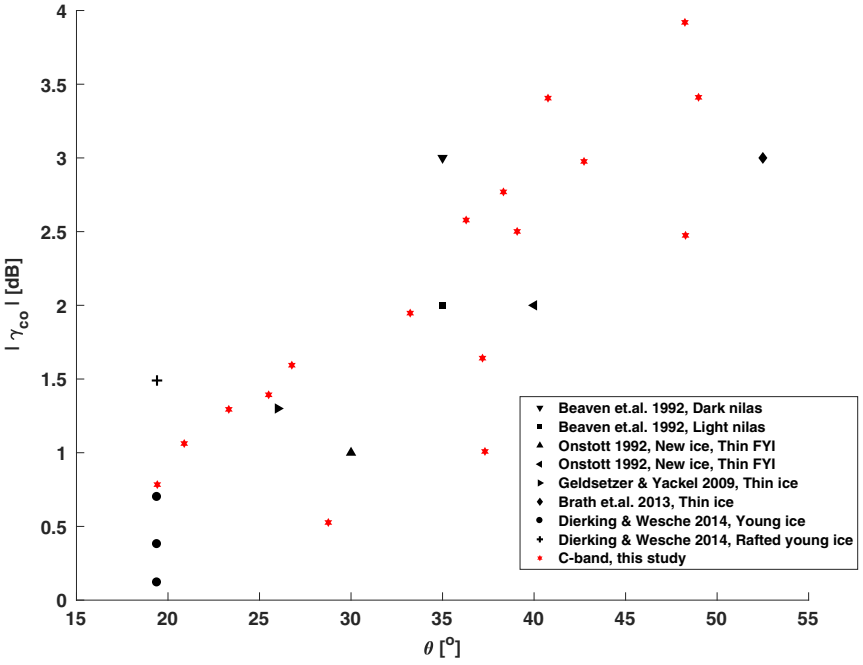

Fig. 11. $|\gamma_{co}|$ values for newly formed sea ice extracted from C-band satellite scenes. Studies by others are presented in black markers and data from this study are presented with red stars. (For interpretation of the references to colour in this figure legend, the reader is referred to the web version of this article.)

Comparing our scattering entropy versus incidence angle results to those from other studies (see Fig. 14) we observe a similar trend, where increased incidence angle corresponds to increased H values. Our study extends the previous studies to X- and L-band frequencies and adds a large number of additional data points to the H versus incidence angle space. Note that the study by Wakabayashi et al. (2004) includes H values for multiple incidence angles at L-band. Results by Dierking and Wesche (2014) show a similar trend to our study where the H values observed in Fig. 14 correspond to α values of 13.38°, 13.71° and 15.78° for young ice and 10.35° for rafted thin ice. This is similar though slightly lower than the α values observed here.

Considering the results from the scattering entropy values and the satellite missions investigated here we argue that incidence angles below 35° are preferable for accurate identification of newly formed sea ice. This is valid for both the X- and C-band SAR, though the effect of the noise floor is more pronounced in the X-band data. Due to this the actual values of the scattering entropy results should be treated with care for the X-band results. The dependence on incidence angle is less pronounced in the L-band SAR and hence using this frequency can add valuable information.

5.4. Is there a temperature dependence in the polarimetric data?

In this study satellite data were acquired when surface temperatures ranged from −31 °C to +1 °C. The drift campaign ended just when the melt season started and therefore this study is not able to address the advanced melt and freeze up season. Within this study, we do not address the physical changes to the sea ice and overlaying snow surface during melt onset and advance melt, but refer to excellent work by, e.g., Casey et al. (2016), Gill et al. (2013, 2015), and Geldsetzer and Yackel

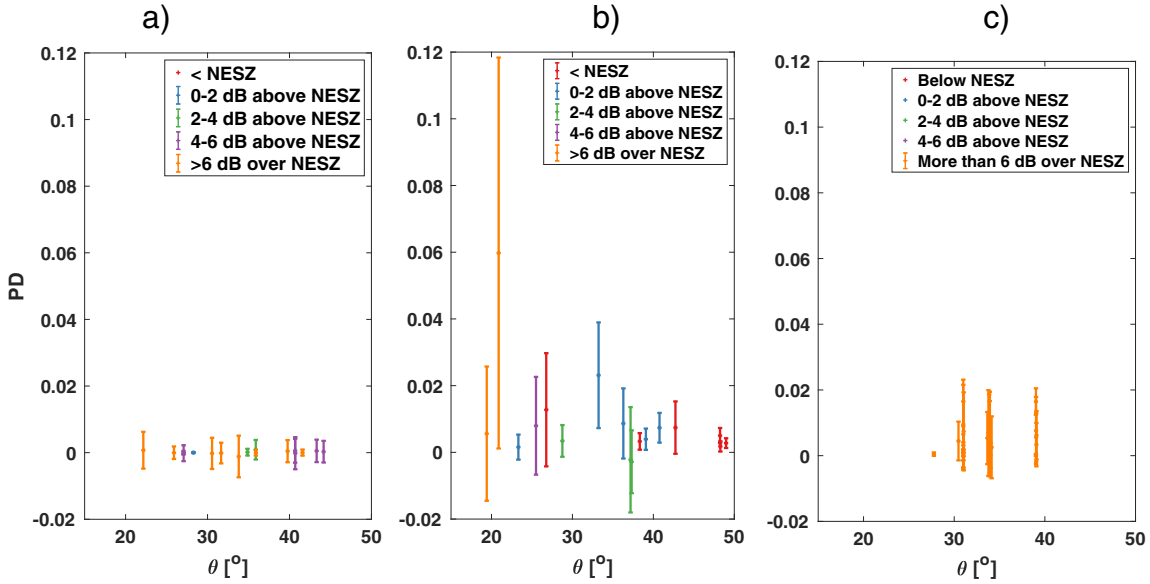

Fig. 12. *PD* values versus θ for a) X-band, b) C-band, and c) L-band. The colours on the lines corresponds to the mean σ^0_{HH} minus one standard deviation above the NESZ for each scene. (For interpretation of the references to colour in this figure legend, the reader is referred to the web version of this article.)

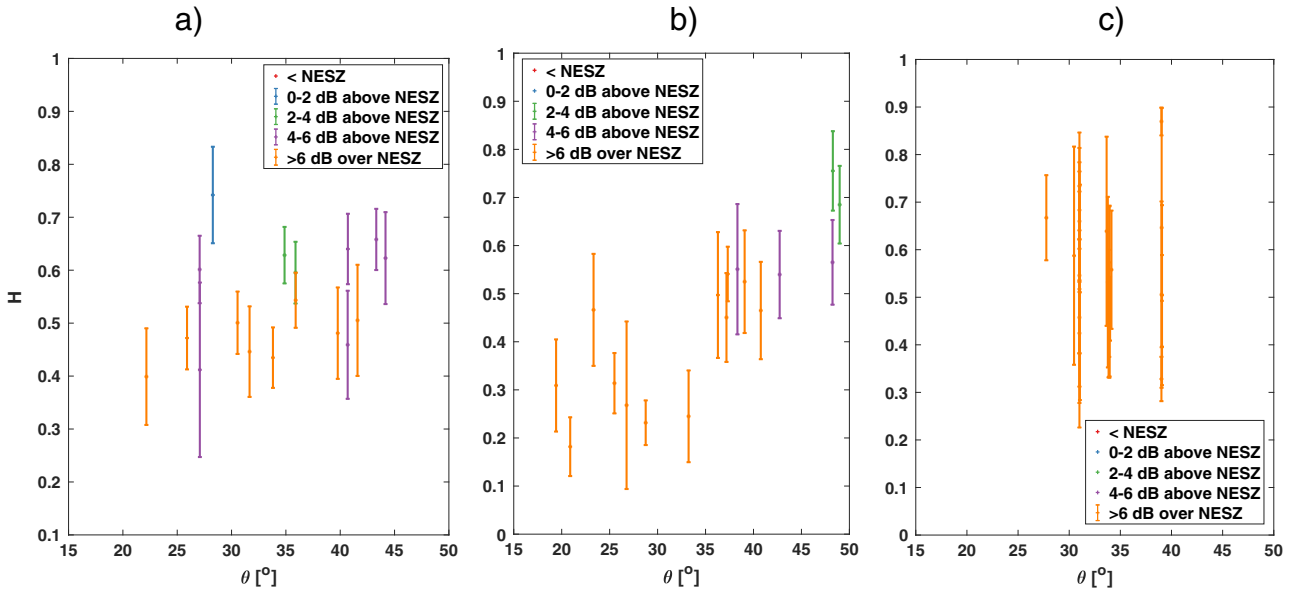

Fig. 13. Scattering entropy H values versus the incidence angle for a) X-band, b) C-band, and c) L-band. The colours on the lines corresponds to the mean σ^0_{HH} minus one standard deviation above the NESZ for each scene. (For interpretation of the references to colour in this figure legend, the reader is referred to the web version of this article.)

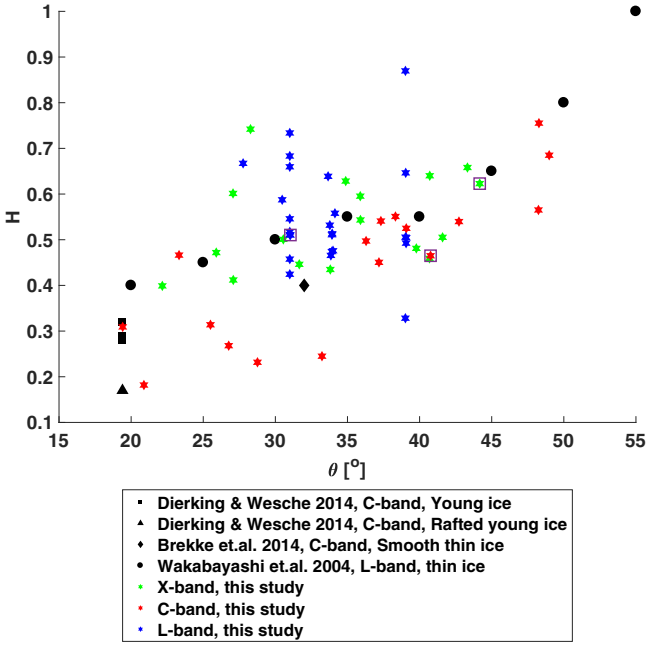

Fig. 14. H values for newly formed sea ice from other studies are presented in black markers. H values for this study are presented in green (X-band), red (C-band), and blue (L-band) stars. Data from the overlapping day, 28 April 2015, is marked by purple squares. (For interpretation of the references to colour in this figure legend, the reader is referred to the web version of this article.)

(2009) and for the dry season to Nghiem et al. (1995). Casey et al. (2016) address changes in backscatter for C- and L-band SAR over first-year ice and multi-year ice during the year as a consequence of melting and freeze-up and Geldsetzer and Yackel (2009) addresses physical changes to thin ice. Using two spatially overlapping fully-polarimetric RADARSAT-2 scenes, one acquired at −7.9 °C and the other at +0.4 °C, Gill et al. (2013) found that over first-year ice the backscatter values and the co-polarization ratios remained consistent within the two scenes. The scattering entropy values had a medium level of consistency and the α values had a low consistency (Gill et al., 2013). Within this study, we investigate whether or not there is an influence of temperature on $|\gamma_{co}|$, H and PD for the dry season and the initial melt season.

As already seen in Section 5.2, a dependence between $|\gamma_{co}|$ and θ for C-band and in Section 5.3 there is a dependence between incidence angle and H values for both X- and C-band. It is important to note that satellite scenes during the warmer conditions were generally acquired with a higher incidence angle. Given that the X-band data have less of an incidence angle dependence for $|\gamma_{co}|$ compared to H we chose to focus on the $|\gamma_{co}|$ values. In Fig. 15, the already established dependence of the data on incidence angle is reflected in the colouration of the bars. A potential increase in $|\gamma_{co}|$ with temperature can be observed from −10 °C for all three frequency data sets, however, due to the incidence angle dependence it is not possible to conclude that the changed $|\gamma_{co}|$ values are an effect of the temperature change. Moreover, the higher temperature values may also be affected by closeness to the NESZ. This trend is also reflected in the H values, where the highest scattering entropy values are related to the highest temperatures. The PD values show no trend related to the temperature and therefor have the potential to be used throughout the winter without taking the temperature influence into account. Overall, for below +1 °C we do not find clear evidence of a temperature dependence for any of the investigated polarimetric parameters for the newly formed sea ice areas.

Summarising our finding, we find no temperature dependence for the polarimetric features studied here. Though for future studies when the temperatures are above −10 °C the incidence angles should if possible be kept below 35°, as doing so may ensure a higher SNR in the acquired data. This is valid for all the studied frequencies here, X-, C- and L-band, though especially valid for C-band.

6. Implications for the monitoring of sea ice for operational use

Using the established sea ice monitoring parameter, γ_{co}, we observe a clear separation of the newly formed sea ice from surrounding thicker sea ice and from the open water (Fig. 6) for C- and L-band. For X-band there is a clear separation between the newly formed sea ice from surrounding thicker sea ice. Due to the incidence angle dependency for C-band (Fig. 10) we investigated three additional polarimetric parameters to see if they could help improve identification and separation of newly formed sea ice from other ice types and open water. Scattering entropy and α values are sometimes (Brekke et al., 2014; Dierking and Wesche, 2014; Wakabayashi et al., 2004), though not regularly, used for sea ice detection, however, they are regularly used to detect similar low backscatter features such as oil spills (Skrunes et al., 2015). The

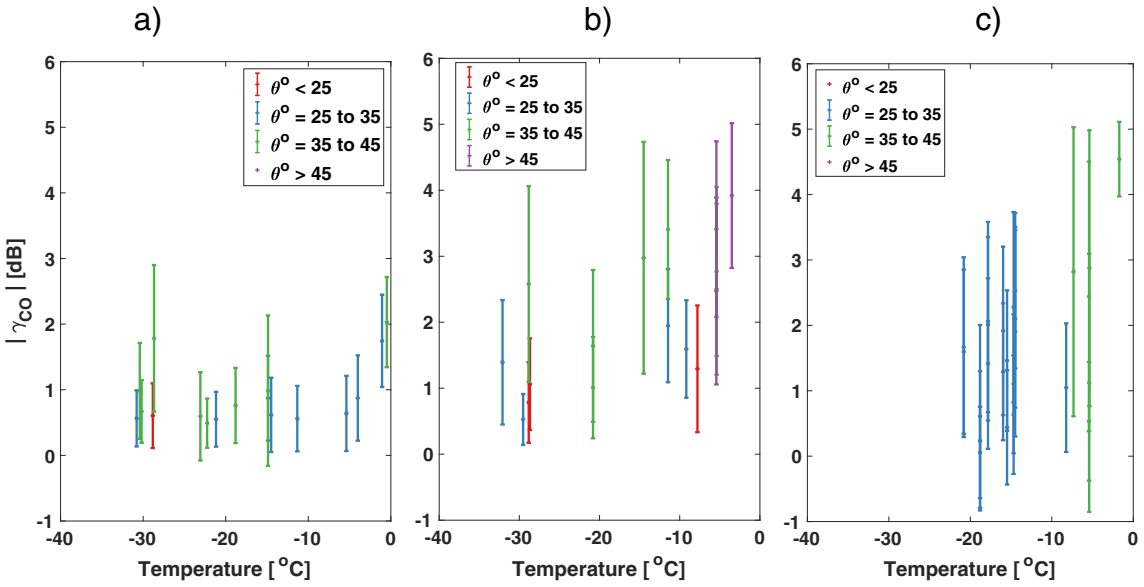

Fig. 15. $|\gamma_{co}|$ values versus temperature for a) X-band, b) C-band, and c) L-band. The colours on the lines corresponds to the incidence angle for each scene. (For interpretation of the references to colour in this figure legend, the reader is referred to the web version of this article.)

lack of incidence angle dependence (Fig. 12) and proven usefulness in oil spill detection (Kudryavtsev et al., 2013) means that *PD* may be able to provide complementary information. Moreover, the compact polarimetry approximate equivalent of *PD*, the Stokes vector second component, has proved useful in separation of first-year sea ice from open water (Dabboor and Geldsetzer, 2014). Within compact polarimetry studies the inclusion of the right co-polarized ratio (approximately equivalent to the co-polarization ratio) was found useful to separate thick first-year ice from grey/grey-white sea ice (Geldsetzer et al., 2015) and the α (CP) parameter (Cloude et al., 2012) was found to improve separation between new ice and thick first-year ice (Geldsetzer et al., 2015). During freeze-up, the degree of polarization (similar to the scattering entropy) and the right co-polarized ratio were useful in separating new sea ice from open water (Geldsetzer et al., 2015).

From the 25 L-band SAR scenes used in this study, we argue that both γ_{co} and H can individually be used to reliably identify newly formed sea ice within L-band SAR. A combination of the two provides additional information about the surface structure and sea ice thickness of the sea ice, i.e., they are complementary features. We observe that the H values can be used to separate the deformed newly formed sea ice from the smooth newly formed sea ice (Fig. 7). Earlier studies by, e.g., Dierking (2010) and Eriksson et al. (2010), both found that deformed sea ice was easier to separate from smooth sea ice with L-band SAR compared to C- and X-band SAR. Separating deformed newly formed sea ice from deformed multi-year ice is important for safe maritime operations. Using a combination of γ_{co} and H for L-band SAR may enable us to do so, and is something that should be investigated further. Wetness is known to affect the backscatter signal and Casey et al. (2016) and Eriksson et al. (2010) found that L-band is less sensitive to snow wetness compared to C- and X-band. This potentially makes it the preferred frequency during the initial stages of the melt season (we do not observe any melt cases in this study). However, L-band SAR scenes are at present not routinely acquired over the Arctic Ocean on a daily basis though with future additional upcoming L-band missions such as ALOS-4 this may change.

For C-band SAR both γ_{co} and H individually are good separators, however, the incidence angle dependency limit their usefulness when $\theta > 35^{\circ}$. The *PD* values show a limited incidence angle dependence (Fig. 12) and as such can replace γ_{co} when the incidence angles are $\theta > 35^{\circ}$ provided there is a sufficiently high SNR. The existing daily acquisitions of C-band over the Arctic, though often with the HH and HV channels, provides a long data record as well as plenty of scenes with different incidence angles. Combined with the extensive validation of these satellite data any decision support method should take C-band data into account even during the melt season.

The X-band SAR scenes used in this study were more affected by SNR and the smaller penetration depth makes it more sensitive to the thinner newly formed sea ice types (Fig. 8). The smaller penetration depth compared to C- and L-band implies that a combination of at least X- and L-band may provide additional information about the actual sea ice thickness. In Fig. 8 a combination of both γ_{co} and H enables us to extract information about the entire width of the lead. Despite the low SNR in the middle (Panel II) the γ_{co} enables separation of this part of the lead, while the H values enable identification of the width of the lead (Panels I and III).

7. Conclusions

Within this study, we have extracted polarimetric information of newly formed sea ice from a six month time series of 59 multi-frequency SAR scenes. We have investigated dual-polarization X-band and quad-polarization C- and L-band SAR response with respect to the co-polarization ratio, scattering entropy, and polarization difference. The overlap between the different frequency data sets enables us to compare the signature from newly formed sea ice at the different frequencies. We have made use of AEM measurements of ice thickness with corresponding photos to confirm the type of newly formed sea ice observed in the SAR scenes.

The co-polarization ratio has successfully been used in previous studies to discriminate newly formed sea ice from the surrounding sea ice and open water, though significant variations within the newly formed sea ice class was observed. We observe that including information about the scattering mechanisms can further improve the discrimination of the classes within the three different frequency data sets. We reduce the C- and L-band data to dual-polarization (HH and VV) data and recalculate the scattering entropy. Comparing the dual- and the quad-polarization scattering entropies we find a high correlation over newly formed sea ice, i.e., little information is lost by the dimensionality reduction, and we can therefore compare the scattering entropy values for all three frequencies. The smaller penetration depth of X-band SAR makes it more sensitive to an increase in sea ice

thickness at the early stages of sea ice growth and by combining X- and L-band SAR we can separate the early stages from the later stages.

Furthermore, the low backscatter over some of the newly formed sea ice areas means that the SNR is not always sufficiently high, particularly for the cross-polarization channels, for characterisation of the newly formed sea ice though it may contain enough information for detection. We therefore recommend that SNR for the cross-polarization channels are calculated before use, and if the SNR is not sufficiently high that the cross-polarization channels are removed over such areas when the aim is to characterise the newly formed sea ice. For the current Sentinel-1A and 1B acquisitions at C-band, this would mean that in many cases only a single co-polarization channel is left for detection of ice covered leads. For the discrimination of open leads, especially wind roughened ones, the cross-polarization channel will still be useful.

This study uses SAR images spanning different incidence angles and we observe that the co-polarization ratio and the scattering entropy values show an incidence angle dependence within the C-band data and to some degree for the X-band data. An automatic system identifying newly formed sea ice therefore needs to take into account the incidence angle. For both the co-polarization ratio and the scattering entropy we recommend that incidence angles below 35° are used to ensure a sufficiently high enough SNR. The polarimetric difference lacks this incidence angle dependence and can therefore be a useful additional parameter to include in an operational automatic system.

By using the co-polarization channels (HH + VV) we can for all three frequencies, provided that the SNR is satisfactory, ensure accurate discrimination of newly formed sea ice from the surroundings. Therefore, X (dual)- and L (quad)-band SAR scenes can be used as additional information to C-band SAR scenes for manual sea ice chart productions and as input into automatic sea ice type analysis.

Acknowledgement

The ALOS-2 Palsar-2 scenes were provided by JAXA under the 4th Research Announcement program (PI: Torbjørn Eltoft, ALOS PI No.1199). RADARSAT-2 data was provided by NSC/KSAT under the Norwegian-Canadian Radarsat agreement 2015. TerraSAR-X images were provided by the German Aerospace Center (DLR) through TerraSAR-X AO OCE2582.

This work has been supported by the Norwegian Polar Institutes Centre for Ice, Climate and Ecosystems (ICE) through the N-ICE project. The work has been supported by the Norwegian Research Council project; Centre for Integrated Remote Sensing and Forecasting for Arctic Operations (CIRFA) (NFR project number 237906). A.M. Johansson has been funded by the Norwegian Research Council (NFR) through the NORRUSS program (NFR project number 233896). G. Spreen was supported by the Institutional Strategy of the University of Bremen, funded by the German Excellence Initiative. J. A. King has been funded by the Norwegian Research Council project CORESAT (NFR project number 222681). This work also benefitted from support from the ESA SMOSIce project (ESA contract 4000110477/14/NL/FF/lf), and from ID Arctic, a project funded by the Norwegian Ministries of Foreign Affairs and Climate and Environment.

The authors wish to thank the personnel from UiT The Arctic University of Norway and the Norwegian Polar Institute who made the co-located satellite image acquisitions and AEM surveys possible; in particular we recognise the efforts of Max König, Marius Bratrein (both NPI) and Thomas Kræmer (UiT), and the TerraSAR-X/TanDEM-X science coordination team.

The authors also extend their thanks to all who participated in the N-ICE2015 campaign; including personnel from the Norwegian Polar Institute as well as many partner organisations, the R/V Lance crew and the Airlift AS helicopter crew.

Appendix A

Table A1

Properties of the TerraSAR-X scenes. The NESZ is the mean value for the HH and VV channel averaged over the entire scene. * marks scenes acquired in descending mode. Non-marked scenes were acquired in ascending mode.

Date	Time (UTC)	Incidence angle (°)	NESZ (dB)
2015-01-28*	08:09	25.1–26.7	−25.22
2015-02-07	14:43	40.1–41.3	−22.49
2015-02-12	14:51	40.1–41.3	−21.80
2015-02-17*	07:09	33.1–34.5	−23.60
2015-02-25*	06:26	39.2–40.4	−22.06
2015-02-28	15:00	41.0–42.2	−21.67
2015-03-14	14:09	35.2–36.6	−23.01
2015-03-20*	07:43	21.3–23.1	−25.64
2015-04-19*	07:00	42.7–43.9	−20.96
2015-04-22	14:00	39.8–31.3	−24.12
2015-04-28*	07:35	30.9–32.4	−23.69
2015-05-01*	06:43	43.6–44.7	−20.70
2015-05-01	14:34	27.5–29.1	−24.71
2015-05-16	15:00	26.2–27.9	−24.63
2015-05-31	15:26	26.3–27.8	−24.84
2015-06-02	14:51	34.2–35.6	−23.01
2015-06-13*	07:01	35.2–36.6	−22.88

Table A2

Properties of the RADARSAT-2 scenes. The NESZ values are the mean values for each scene averaged over the entire scene. * marks scenes acquired in descending mode. Non-marked scenes were acquired in ascending mode.

Date	Time (UTC)	Incidence angle (°)	NESZ (dB)
2015-01-26	13:39	28.1–29.8	−35.31
2015-02-07	12:49	19.7–21.6	−37.21
2015-03-19	13:22	24.5–26.5	−36.20
2015-03-20	12:53	18.4–20.4	−37.59
2015-03-20	14:34	35.5–37.1	−33.91
2015-04-23	14:42	36.5–38.0	−33.38
2015-04-23	14:42	36.5–38.0	−33.38
2015-04-28	15:36	42.0–43.4	−31.43
2015-05-20	14:54	25.8–27.6	−35.91
2015-05-23*	06:47	32.5–34.1	−34.96
2015-05-23*	06:47	40.3–41.7	−32.93
2015-05-24	14:38	22.2–24.1	−36.56
2015-05-26	17:00	47.6–48.8	−31.52
2015-05-26	17:00	48.4–49.5	−31.74
2015-05-27	16:30	38.4–39.9	−33.66
2015-05-30	16:43	48.4–49.5	−31.74
2015-05-31	16:14	37.5–38.9	−33.68

Table A3

Properties of the ALOS-2 scenes. The NESZ is sensor specific for the co-polarization and the cross-polarization channels. All scenes were acquired in ascending mode.

Date	Time (UTC)	Incidence angle (°)	NESZ (dB)
2015-04-19	20:32	32.4–35.4	−36.0 (HH), −46.0 (HV)
2015-04-23	20:18	32.4–35.4	−36.0 (HH), −46.0 (HV)
2015-04-24	20:39	32.4–35.4	−36.0 (HH), −46.0 (HV)
2015-04-24	22:16	32.4–35.4	−36.0 (HH), −46.0 (HV)
2015-04-28	20:25	29.5–32.6	−36.0 (HH), −46.0 (HV)
2015-04-29	20:31	29.5–32.6	−36.0 (HH), −46.0 (HV)
2015-05-04	20:52	29.5–32.6	−36.0 (HH), −46.0 (HV)
2015-05-10	21:20	29.5–32.7	−36.0 (HH), −46.0 (HV)
2015-05-18	20:52	25.7–29.8	−36.0 (HH), −46.0 (HV)
2015-05-25	21:41	37.7–40.3	−36.0 (HH), −46.0 (HV)
2015-05-26	22:02	37.7–40.3	−36.0 (HH), −46.0 (HV)
2015-05-28	21:06	37.7–40.3	−36.0 (HH), −46.0 (HV)
2015-05-31	22:08	37.7–40.3	−36.0 (HH), −46.0 (HV)
2015-06-07	21:19	37.7–40.3	−36.0 (HH), −46.0 (HV)

Appendix B. Supplementary data

Supplementary data to this article can be found online at https://doi.org/10.1016/j.rse.2017.10.032.

References

Airbus Defence & Space, 2014. Radiometric Calibration of TerraSAR-X Data, Beta Naught and Sigma Naught Coefficient Calibration. (TSXX-ITD-TN-0049).

Alexandrov, V.Y., Sandven, S., Kloster, K., Bobylev, L.P., Zaitsev, L.V., 2004. Comparison of sea ice signatures in OKEAN and RADARSAT radar images for the northeastern Barents Sea. Can. J. Remote. Sens. 30 (6), 882–892. http://dx.doi.org/10.5589/m04-048.

Arkett, M., Flett, D., De Abreu, R., Clemente-Colón, P., Woods, J., Melchior, B., 2008. Evaluating ALOS-PALSAR for ice monitoring — what can L-band do for the North American ice service? In: Proc. IEEE IGARSS 2008, Boston, USA, 6–11 July. 5. pp. 188–191. http://dx.doi.org/10.1109/IGARSS.2008.4780059.

Arkett, M., Flett, D., De Abreu, R., Gillespie, C., 2006. Sea ice type and open water discrimination for operational ice monitoring with RADARSAT-2. In: Proc. IEEE IGARSS 2006, Denver, USA, 31 July–4 Aug. pp. 1631–1634. http://dx.doi.org/10.1109/IGARSS.2006.421.

Assmy, P., Fernández-Méndez, M., Duarte, P., Meyer, A., Randelhoff, A., Mundy, C.J., Olsen, L.M., Kauko, H., Bailey, A., Chierici, M., Cohen, L., Doulgeris, A.P., Ehn, J.K., Fransson, A., Gerland, S., Hop, H., Hudson, S.R., Hughes, N., Itkin, P., Johnsen, G., King, J., Koch, B.P., Koenig, Z., Kwasniewski, S., Laney, S.R., Nicolaus, M., Pavlov, A., Polashenski, C.M., Provost, C., Rösel, A., Sandbu, M., Spreen, G., Smedsrud, L.H., Sundfjord, A., Taskjelle, T., Tatarek, A., Wiktor, J., Wagner, P.M., Wold, A., Steen, H., Granskog, M.A., 2017. Leads in Arctic pack ice enable early phytoplankton blooms below snow-covered sea ice. Nat. Sci Rep. 7. http://dx.doi.org/10.1038/srep40850.

Beaven, S.G., Gogineni, S.P., Shanableh, M., 1993. Young sea ice signatures in the deep Arctic during the fall freeze-up. In: Proc. IEEE IGARSS 1993, Tokyo, Japan, 18–21 Aug. 2. pp. 434–436. http://dx.doi.org/10.1109/IGARSS.1993.322312.

Brath, M., Kern, S., Stammer, D., 2013. Sea ice classification during freeze-up conditions with multifrequency scatterometer data. IEEE Trans. Geosci. Remote Sens. 51 (6),

3336–3353. http://dx.doi.org/10.1109/TGRS.2012.2222031.
Brekke, C., Holt, B., Jones, C., Skrunes, S., 2014. Discrimination of oil spills from newly formed sea ice by synthetic aperture radar. Remote Sens. Environ. 145, 1–14. http://dx.doi.org/10.1016/j.rse.2014.01.015.
Carlström, A., Ulander, L.M.H., 1995. Validation of backscatter models for level and deformed sea-ice in ERS-l SAR images. Int. J. Remote Sens. 16 (17), 3245–3266. http://dx.doi.org/10.1080/01431169508954629.
Casey, J.A., Howell, S.E.L., Tivy, A., Haas, C., 2016. Separability of sea ice types from wide swath C- and L-band synthetic aperture radar imagery acquired during the melt season. Remote Sens. Environ. 174, 314–328. http://dx.doi.org/10.1016/j.rse.2015.12.021.
Cloude, S.R., Goodenough, D.G., Chen, H., 2012. Compact decomposition theory. IEEE Geosci. Remote Sens. Lett. 9 (1), 28–32. http://dx.doi.org/10.1109/LGRS.2011.2158983.
Cloude, S.R., Pottier, E., 1997. An entropy based classification scheme for land applications of polarimetric SAR. IEEE Trans. Geosci. Remote Sens. 35 (1), 68–78. http://dx.doi.org/10.1109/36.551935.
Cohen, L., Hudson, S.R., Walden, V.P., Graham, R.M., Granskog, M.A., 2017. Meteorological conditions in a thinner Arctic sea ice regime from winter through summer during the Norwegian young sea ICE expedition (N-ICE2015). J. Geophys. Res. Atmos. 122 (14), 7235–7259. http://dx.doi.org/10.1002/2016JD026034.
Dabboor, M., Geldsetzer, T., 2014. Towards sea ice classification using simulated RADARSAT Constellation Mission compact polarimetric SAR imagery. Remote Sens. Environ. 140, 189–195. http://dx.doi.org/10.1016/j.rse.2013.08.035.
Dierking, W., 2010. Mapping of different sea ice regimes using images from Sentinel-1 and ALOS synthetic aperture radar. IEEE Trans. Geosci. Remote Sens. 48 (3), 1045–1058. http://dx.doi.org/10.1109/TGRS.2009.2031806.
Dierking, W., Wesche, C., 2014. C-band radar polarimetry useful for detection of icebergs in sea ice? IEEE Trans. Geosci. Remote Sens. 52 (1), 25–37. http://dx.doi.org/10.1109/TGRS.2012.2234756.
Dierking, W., Busche, T., 2006. Sea ice monitoring by L-band SAR: an assessment based on literature and comparisons of JERS-1 and ERS-1 imagery. IEEE Trans. Geosci. Remote Sens. 44 (4), 957–970. http://dx.doi.org/10.1109/TGRS.2005.861745.
Dierking, W., Pettersson, M.I., Askne, J., 1999. Multifrequency scatterometer measurements of Baltic Sea ice during EMAC-95. Int. J. Remote Sens. 20 (2), 349–372. http://dx.doi.org/10.1080/014311699213488.
Doulgeris, A.P., 2013. A Simple and Extendable Segmentation Method for Multi-Polarisation SAR Images. In: Proc. POLinSAR 2013, Frascati, Italy, pp. 8.
Doulgeris, A.P., Eltoft, T., 2010. Scale mixture of Gaussian modelling of polarimetric SAR data, EURASIP. J. Appl. Signal Process. 2010 (874592), 12. http://dx.doi.org/10.1155/2010/874592.
Drinkwater, M.R., Kwok, R., Winebrenner, D.P., Rignot, E., 1991. Multifrequency polarimetric synthetic aperture radar observations of sea ice. J. Geophys. Res. 96 (C11), 20679–20698. http://dx.doi.org/10.1029/91JC01915.
Eriksson, L.E.B., Borenäs, K., Dierking, W., Berg, A., Santoro, M., Pemberton, P., Lindh, H., Karlson, B., 2010. Evaluation of new spaceborne SAR sensors for sea-ice monitoring in the Baltic Sea. Can. J. Remote. Sens. 36 (1), S56–S73. http://dx.doi.org/10.5589/m10-020.
Espeseth, M.M., Brekke, C., Johansson, A.M., 2017. Assessment of RISAT-1 and RADARSAT-2 for sea ice observations from a hybrid-polarity perspective. Remote. Sens. 9. http://dx.doi.org/10.3390/rs9111088.
Freeman, A., Durden, S.L., 1998. A three-component scattering model for polarimetric SAR data. IEEE Trans. Geosci. Remote Sens. 36 (3), 963–973. http://dx.doi.org/10.1109/36.673687.
Geldsetzer, T., Arkett, M., Zagon, T., Charbonneau, F., Yackel, J.J., Scharien, R.K., 2015. All-season compact-polarimetry C-band SAR observations of sea Ice. Can. J. Remote. Sens. 41 (5), 485–504. http://dx.doi.org/10.1080/07038992.2015.1120661.
Geldsetzer, T., Yackel, J.J., 2009. Sea ice type and open water discrimination using dual co-polarized C-band SAR. Can. J. Remote. Sens. 35 (1), 73–84. http://dx.doi.org/10.5589/m08-075.
Gerland, S., Granskog, M.A., King, J., Rösel, A., 2017. N-ICE2015 Ice Core Physics: Temperature, Salinity and Density [Data set]. Norwegian Polar Institutehttp://dx.doi.org/10.21334/npolar.2017.c3db82e3.
Gill, J.P.S., Yackel, J.J., 2012. Evaluation of C-band SAR polarimetric parameters for discrimination of first-year sea ice types. Can. J. Remote. Sens. 38 (3), 306–323. http://dx.doi.org/10.5589/m12-025.
Gill, J.P.S., Yackel, J.J., Geldsetzer, T., 2013. Analysis of consistency in first-year sea ice classification potential of C-band SAR polarimetric parameters. Can. J. Remote. Sens. 39 (2), 101–117. http://dx.doi.org/10.5589/m13-016.
Gill, J.P.S., Yackel, J.J., Geldsetzer, T., Fuller, M.C., 2015. Sensitivity of C-band synthetic aperture radar polarimetric parameters to snow thickness over landfast first-year sea ice. Remote Sens. Environ. 166, 34–49. http://dx.doi.org/10.1016/j.rse.2015.06.005.
Granskog, M.A., Assmy, P., Gerland, S., Spreen, G., Steen, H., Smedsrud, L.H., 2016. Arctic research on thin ice: consequences of Arctic Sea ice loss. Eos Trans. AGU 97 (5), 22–36. http://dx.doi.org/10.1029/2016EO044097.
Granskog, M.A., Rösel, A., Dodd, P.A., Divine, D., Gerland, S., Martma, T., Leng, M.J., 2017. Snow contribution to first-year and second-year Arctic Sea ice mass balance north of Svalbard. J. Geophys. Res. Oceans 122 (3), 2539–2549. http://dx.doi.org/10.1002/2016JC012398.
Haas, C., Lobach, J., Hendricks, S., Rabenstein, L., Pfaffling, A., 2009. Helicopter-borne measurements of sea ice thickness, using a small and lightweight, digital EM system. J. Appl. Geophys. Airborne Geophys. 67, 234–241. http://dx.doi.org/10.1016/j.jappgeo.2008.05.005.
Hallikainen, M., Winebrenner, D.P., 1992. The Physical Basis for Sea Ice Remote Sensing. In: Carsey, F.D. (Ed.), Microwave Remote Sensing of Sea Ice. American Geophysical Union, Washington, D.C., pp. 68. http://dx.doi.org/10.1029/GM068p0029.
Hudson, S., Cohen, L., Walden, V.P., 2015. N-ICE2015 Surface Meteorology v2 [Data set]. Norwegian Polar Institutehttp://dx.doi.org/10.21334/npolar.2015.056a61d1.
Isleifson, D., Galley, R.J., Barber, D.G., Landy, J.C., Komarov, A.S., Shafai, L., 2014. A study on the C-Band polarimetric scattering and physical characteristics of frost flowers on experimental sea ice. IEEE Trans. Geosci. Remote Sens. 52 (3), 1787–1798. http://dx.doi.org/10.1109/TGRS.2013.2255060.
Itkin, P., Spreen, G., Cheng, B., Doble, M., Gerland, S., Granskog, M.A., Haapala, J., Hudson, S.R., Kaleschke, L., Nicolaus, M., Pavlov, A., Steen, H., Wilkinson, J., Helgeland, C., 2015. N-ICE2015 Buoy Data [Data set]. Norwegian Polar Institutehttp://dx.doi.org/10.21334/npolar.2015.6ed9a8ca.
Johansson, A.M., Brekke, C., Spreen, G., King, J.A., Gerland, S., 2016. Newly formed sea ice in the Arctic leads monitored by C- and L-band SAR. In: Proc. ESA Living Planet Symp. 9–13 May, 2016, Prague, Czech Republic, ESA-SP. vol. 740 (8 pp.).
Johansson, A.M., King, J.A., Doulgeris, A.P., Gerland, S., Singha, S., Spreen, G., Busche, T., 2017. Combined observations of Arctic sea ice with near-co-incident X-band, C-band, and L-band SAR satellite remote sensing and helicopter-borne measurements. J. Geophys. Res. Oceans 122, 669–691. http://dx.doi.org/10.1002/2016JC012273.
Kaleschke, L., Tian-Kunze, X., Maaß, N., Mäkynen, M., Drusch, M., 2012. Sea ice thickness retrieval from SMOS brightness temperatures during the Arctic freeze-up period. Geophys. Res. Lett. 39, L05501. http://dx.doi.org/10.1029/2012GL050916.
Kern, S., Gade, M., Haas, C., Pfaffling, A., 2006. Retrieval of thin-ice thickness using the L-band polarization ratio measured by the helicopter-borne scatterometer HELISCAT. Ann. Glaciol. 44 (1), 275–280. http://dx.doi.org/10.3189/172756406781811880.
King, J.A., Gerland, S., Spreen, G., Bratrein, M., 2016. N-ICE2015 Sea-ice Thickness Measurements from Helicopter-borne Electromagnetic Induction Sounding [Data set]. Norwegian Polar Institutehttp://dx.doi.org/10.21334/npolar.2016.aa3a5232.
Kudryavtsev, V.N., Chapron, B., Myasoedov, A.G., Collard, F., Johannessen, J.A., 2013. On dual co-polarized SAR measurements of the ocean surface. IEEE Geosci. Remote Sens. Lett. 10 (4), 761–765. http://dx.doi.org/10.1109/LGRS.2012.2222341.
Lee, J.S., Pottier, E., 2009. Polarimetric Radar Imaging, From Basics to Applications. CRC Press, Taylor and Francis Group, Boca Raton, USA.
Lehtiranta, J., Siiriä, S., Karvonen, J., 2015. Comparing C- and L-band SAR images for sea ice motion estimation. Cryosphere 9, 357–366. http://dx.doi.org/10.5194/tc-9-357-2015.
Lundhaug, M., 2002. ERS SAR studies of sea ice signatures in the Pechora Sea and Kara Sea region. Can. J. Remote. Sens. 28 (2), 114–127. http://dx.doi.org/10.5589/m02-022.
MacDonald, Dettwiler and Associates Ltd, 2016. RADARSAT-2 Product Description, Richmond, BC, USA, RN-SP-52-1238, Issue 1/13: March 21. pp. 2016.
MacDonald, Dettwiler and Associates Ltd, 2016. RADARSAT-2 Product Format Definition, Richmond, BC, USA, RN-SP-51-2713, Issue 1/15: Oct. 26. pp. 2016.
Maillard, P., Clausi, D.A., Deng, H., 2005. Operational map-guided classification of SAR sea ice imagery. IEEE Trans. Geosci. Remote Sens. 43 (12), 2940–2951. http://dx.doi.org/10.1109/TGRS.2005.857897.
Markus, T., Stroeve, J.C., Miller, J., 2009. Recent changes in Arctic Sea ice melt onset, freezeup, and melt season length. J. Geophys. Res. 114, C12024. http://dx.doi.org/10.1029/2009JC005436.
Martin, S., Drucker, R., Fort, M., 1995. A laboratory study of frost flower growth on the surface of young sea ice. J. Geophys. Res. Oceans 100 (C4), 7027–7036. http://dx.doi.org/10.1029/94JC03243.
Martin, S., Drucker, R., Kwok, R., Holt, B., 2004. Estimation of the thin ice thickness and heat flux for the Chukchi Sea Alaskan coast polynya from Special Sensor Microwave/Imager data, 1990–2001. J. Geophys. Res. 109, C10012. http://dx.doi.org/10.1029/2004JC002428.
Minchew, B., Jones, C.E., Holt, B., 2012. Polarimetric analysis of backscatter from the Deepwater Horizon oil spill using L-band synthetic aperture radar. IEEE Trans. Geosci. Remote Sens. 50 (10), 3812–3830. http://dx.doi.org/10.1109/TGRS.2012.2185804.
Moen, M.-A.N., Anfinsen, S., Doulgeris, A.P., Renner, A.H.H., Gerland, S., 2015. Assessing polarimetric SAR sea-ice classifications using consecutive day images. Ann. Glaciol. 56 (69), 285–294. http://dx.doi.org/10.3189/2015AoG69A802.
Moen, M.A.N., Doulgeris, A.P., Anfinsen, S., Renner, A.H.H., Hughes, N., Gerland, S., Eltoft, T., 2013. Comparison of automatic segmentation of full polarimetric SAR sea ice images with manually drawn ice charts. Cryosphere 7 (6), 1693–1705. http://dx.doi.org/10.5194/tc-7-1693-2013.
Nakamura, K., Wakabayashi, H., Naoki, K., Nishio, F., Moriyama, T., Uratsuka, S., 2005. Observation of sea-ice thickness in the Sea of Okhotsk by using dual-frequency and fully polarimetric airborne SAR (Pi-SAR) data. IEEE Trans. Geosci. Remote Sens. 43 (11), 2460–2469. http://dx.doi.org/10.1109/TGRS.2005.853928.
Nghiem, S.V., Bertoia, C., 2001. Multi-polarization C-band SAR signatures of Arctic Sea ice. Can. J. Remote. Sens. 27 (5), 387–402. http://dx.doi.org/10.1080/07038992.2001.10854882.
Nghiem, S.V., Kwok, R., Yueh, S.H., Drinkwater, M.R., 1995. Polarimetric signatures of sea ice 2. Experimental observations. J. Geophys. Res. 100 (C7), 13681–13698. http://dx.doi.org/10.1029/95JC00938.
Nghiem, S.V., Kwok, R., Yueh, S.H., Gow, A.V., Perovich, D.K., Kong, J.A., Hsu, C.C., 1997. Evolution in polarimetric signatures of thin saline ice under constant growth. Radio Sci. 32 (1), 127–151. http://dx.doi.org/10.1029/96RS03051.
Oliver, C., Quegan, S., 2004. Understanding Synthetic Aperture Radar Images. SciTech Publishing Inc., Raleigh, USA.
Onstott, R.G., 1992. SAR and scatterometer signatures of sea ice chapter 5. In: Carsey, F.D. (Ed.), Microwave Remote Sensing of Sea Ice. American Geophysical Union, Washington D.C., pp. 77–104. http://dx.doi.org/10.1029/GM068p0073.
Partington, K.C., Flach, J.D., Barber, D., Isleifson, D., Meadows, P.J., Verlaan, P., 2010.

Dual-polarization C-band radar observations of sea ice in the Amundsen Gulf. IEEE Trans. Geosci. Remote Sens. 48 (6), 2685–2691. http://dx.doi.org/10.1109/TGRS.2009.2039577.

Raney, R.K., 2007. Hybrid-polarity SAR architecture. IEEE Trans. Geosci. Remote Sens. 45 (11), 3397–3404. http://dx.doi.org/10.1109/TGRS.2007.895883.

Ressel, R., Singha, S., 2016. Comparing near coincident space borne C and X band fully polarimetric SAR data for Arctic Sea ice classification. Remote Sens. 8 (3), 198. http://dx.doi.org/10.3390/rs8030198.

Rösel, A., Divine, D., King, J.A., Nicolaus, M., Spreen, G., Itkin, P., Polashenski, C.M., Liston, G.E., Ervik, Å., Espeseth, M., Gierisch, A., Haapala, J., Maaß, N., Oikkonen, A., Orsi, A., Shestov, A., Wang, C., Gerland, S., Granskog, M., 2016. N-ICE2015 Total (Snow and Ice) Thickness Data from EM31 [Data set]. Norwegian Polar Institutehttp://dx.doi.org/10.21334/npolar.2016.70352512.

Sandven, S., Kloster, K., Alexandrov, V., Piotrovskaya, N., Zakhvatkina, N., 2008. Sea Ice Classification Using ASAR Alternating Polarisation Images. In: SeaSAR 2008, 21–24 January 2008, Oslo, Norway.

Scheuchl, B., Flett, D., Caves, R., Cumming, I., 2004. Potential of RADARSAT-2 data for operational sea ice monitoring. Can. J. Remote. Sens. 30 (3), 448–461. http://dx.doi.org/10.5589/m04-011.

Shimada, M., Isoguchi, O., Tadono, T., Isono, K., 2009. PALSAR radiometric and geometric calibration. IEEE Trans. Geosci. Remote Sens. 47 (12), 3915–3932. http://dx.doi.org/10.1109/TGRS.2009.2023909.

Shimada, M., M., Watanabe,Motooka, T., Kankaku, Y., Suzuki, S., 2015. Calibration and validation of the PALSAR-2. In: Proc. IEEE IGARS 2015, Milan, Italy, 26–31 July.

Shokr, M., 2009. Compilation of a radar backscatter database of sea ice types and open water using operational analysis of heterogeneous ice regimes. Can. J. Remote. Sens. 35 (4), 369–384. http://dx.doi.org/10.5589/m09-026.

Skrunes, S., Brekke, C., Eltoft, T., 2015. Characterization of marine surface slicks by Radarsat-2 multipolarization features. IEEE Trans. Geosci. Remote Sens. 52 (9), 5302–5319. http://dx.doi.org/10.1109/TGRS.2013.2287916.

Thomas, M., Kambhamettu, C., Geiger, C.A., 2011. Motion tracking of discontinuous sea ice. IEEE Trans. Geosci. Remote Sens. 49 (12), 5064–5079. http://dx.doi.org/10.1109/TGRS.2011.2158005.

Wakabayashi, H., Matsuoka, T., Nakamura, K., Nishio, F., 2004. Polarimetric characteristics of sea ice in the Sea of Okhotsk observed by airborne L-band SAR. IEEE Trans. Geosci. Remote Sens. 42 (11), 2412–2425. http://dx.doi.org/10.1109/TGRS.2004.836259.

Wakabayashi, H., Mori, Y., Nakamura, K., 2013. Sea ice detection in the Sea of Okhotsk using PALSAR and MODIS data. IEEE J. Sel. Top. Appl. Earth Obs. Remote Sens. 6 (3), 1516–1523. http://dx.doi.org/10.1109/JSTARS.2013.2258327.

Wakabayashi, H., Sakai, S., 2010. Estimation of sea ice concentration in the sea of Okhotsk using Palsar polarimetric data. In: Proc. IEEE IGARSS 2010, Honolulu, USA, 25–30 July, pp. 2398–2401. http://dx.doi.org/10.1109/IGARSS.2010.5652440.

Walker, N.P., Partington, K.C., Woert, M.L.V., Street, T.L.T., 2006. Arctic Sea ice type and concentration mapping using passive and active microwave Sensors. IEEE Trans. Geosci. Remote Sens. 44 (12), 3574–3584. http://dx.doi.org/10.1109/TGRS.2006.881116.

Winebrenner, D.P., Farmer, L.D., Joughin, I.R., 1995. On the response of polarimetric synthetic aperture radar signatures at 24-cm wavelength to sea ice thickness in Arctic leads. Radio Sci. 30 (2), 373–402. http://dx.doi.org/10.1029/94RS02313.

World Meteorological Organization, 1970. WMO Sea-Ice Nomenclature: Terminology, Codes and Illustrated Glossary. vol. 259 WMO Publ. (Rev. Mar 2014), 147 pp., Secr. of the World Meteorol. Organ., Geneva, Switzerland.

Zakhvatkina, N., Korosov, A., Muckenhuber, S., Sandven, S., Babiker, M., 2017. Operational algorithm for ice-water classification on dual-polarized RADARSAT-2 images. Cryosphere 11, 33–46. http://dx.doi.org/10.5194/tc-11-33-2017.

Zakhvatkina, N.Y., Alexandrov, V.Y., Johannessen, O.M., Sandven, S., Frolov, I.Y., 2013. Classification of sea ice types in ENVISAT synthetic aperture radar images. IEEE Trans. Geosci. Remote Sens. 51 (5), 2587–2600. http://dx.doi.org/10.1109/TGRS.2012.2212445.

Zhang, X., Dierking, W., Zhang, J., Meng, J., Lang, H., 2016. Retrieval of the thickness of undeformed sea ice from simulated C-band compact polarimetric SAR images. Cryosphere 10, 1529–1545. http://dx.doi.org/10.5194/tc-10-1529-2016.